Eindhoven University of Technology

MASTER

Reduced Order Modeling of Air Bearings

In cooperation with Sioux Mathware

Middelhuis, S.

Award date:
2022

Link to publication

TU/e

SIOUX TECHNOLOGIES

Reduced Order Modeling of Air Bearings

In cooperation with Sioux Mathware

MASTER THESIS

Author: S. Middelhuis
0947014
s.middelhuis@student.tue.nl

This report was made in accordance with the TU/e Code of Scientific Conduct for the Master thesis

Abstract

System models are invaluable in analysing functional modules of complex mechatronic systems. In such models, also called lumped mass models, the components are represented by only a few degrees of freedom. This is often too coarse to get sufficiently accurate or even meaningful results. High fidelity models of these components based on the finite element method, however, often come with great computational cost which for some applications form a significant drawback. At Sioux Mathware, knowledge on systematic and automatic reduction of finite element models to so-called reduced order models (ROMs) for the use in system models is developed. These ROMs may then be used for e.g. real-time FEM simulations in feedback control or as part of a larger FEM simulation. One of the major challenges in creating ROMs is dealing with non-linearities. The dynamic behaviour of gas lubricated journal bearings is an example of a non-linear (on account of, at least, turbulence and convection) system. These bearings are used as rotating/sliding joints for, e.g. the suspension of shafts in turbo-machinery and high precision positioning devices. In this master thesis the development of a finite element model of an air bearing is elaborated. Both model-based and data-driven model order reduction techniques are then utilized to define a ROM of the proposed model.

Contents

List of Figures

Chapter 1

Introduction

System models are invaluable in analysing functional modules of complex mechatronic systems. In such models, also called lumped mass models, the components are represented by only a few degrees of freedom. This is often too coarse to get sufficiently accurate or even meaningful results. High fidelity models of these components based on the finite element method (FEM) form a better and more accurate representation, as these models are physics based and include possible non-linear behaviour. These models, however, often come with great computational cost which for some applications form a significant drawback. At Sioux Mathware, knowledge on systematic and automatic reduction of finite element models to so-called reduced order models (ROMs) for the use in system models is developed. These ROMs may then be used for e.g. real time FEM simulations in feedback control or as part of a larger FEM simulation.

One of the major challenges in creating ROMs is dealing with non-linearities. A commonplace approach is to combine local linearisations (The empirical interpolation method of Maday et al. [1] is a prominent example). Also system theory techniques for model order reduction, e.g. balanced truncation (BT) or iterative rational krylov algorithms (IRKA), are widely used in industry as it integrates well with dynamical system models. A new emerging technique is to take a Koopman operator theory perspective [2]. That is, to find a combination of nonlinear measurements of the system state in which the system appears to behave linearly. Only in the past ten years, starting with the work of Mezić [3], ways are starting to be found to approximate this so-called coordinate transformation that can linearize system response.

The dynamic behaviour of gas lubricated journal bearings is an example of a non-linear (on account of, at least, turbulence and convection) system. These bearings are used as rotating/sliding joints for, e.g. the suspension of shafts in turbo-machinery and high precision positioning devices. Gas lubricated bearings are attractive because of their advantages over traditional oil lubricated systems, namely, minimal friction losses, high durability and environmental friendliness [4]. The dynamic behaviour of gas lubricated bearings is often studied through numerical models based on linearization of the Reynolds equation [5–7]. These models are used to predict the bearing performance in terms of load capacity and stiffness both statically and dynamically. Numerical solutions to these models based on finite element comuptations have been found earlier, e.g. in [8, 9], however only for rotational joints. The dynamic behaviour of the linear horizontal motion of gas lubricated journal bearings is not much covered yet in literature.

1.1   Objective and outline

As stated above, the significant computational cost of a FEM simulation often restricts the use of these models in real time applications. The overarching objective of the research presented in this thesis is therefore the development of reduced order finite element models of gas lubricated

journal bearings. Both system theory and Koopman-based algorithims form a promising approach for divergent reasons, which will therefore be explored. The accuracy of the different ROM approaches to predict dynamic characteristics and its efffiency regarding computational cost will be investigated and compared to the high fidelity results.

In Chapter 2 the geometry of the used journal bearing is ellaborated. This geometry is then used to propose a mathematical framework which will describe the dynamics of a gas lubricated journal bearing. The required assumptions and their inpact to the model, as well as the boundary conditions for the problem will also be discussed.

Chapter 3 includes the discretization of the high fidelity model posed in Chapter 2. A numerical framework is selected to solve the discretized problem for both steady state and transient problems. The convergence of the solution and quantities of interest is investigated to determine the accuracy and quality of this discretization. Additionally, the high fidelity results are presented, discussed and validated using results found in literature.

In Chapter 4 the ROM approach is presented which is used for the reduction of the high fidelity numerical model posed in Chapter 3. Different approaches are selected to demonstrate the differences in accuracy and efficiency. The ROM results are compared to the high fidelity results and validated with literature.

In Chapter 5 the conclusions are drawn and reccomendation for future research are discussed.

Chapter 2

Journal gas bearing model

The main task associated to the modeling of a gas bearing system is to define the gas pressure distribution within the thin lubricating film of the bearing. This pressure distribution expresses upon integration the forces which affect the bearing, subsequently introducing a notion of bearing stiffness. In order to find characteristics such as the bearing stiffness and damping, a finite element model is constructed. This model allows one to solve for the film pressure distribution and find the bearing performance and characteristics as a function of geometrical properties and boundary conditions.

In lubrication theory for in- and compressible lubricants, the pressure distribution of the viscous film is often solved using a thin film approach described by the so called Reynolds equation (Reynolds 1886). It forms a convenient model as the condition of mass continuity is embodied within its definition. Hence there is no need for iterating for mass flow balance as this is implicitly respected. This model is also very well applicable to the gas bearing system considered in this thesis as will later be elaborated further.

The construction of this model regarding the used geometry and the mathematical framework including the governing equations will be discussed in this chapter. The required assumptions to arrive at the Reynolds equation will be elaborated as well as the physical significance of its terms. At last a dimensionless analysis of this air bearing model will be provided to conclude with a complete problem definition.
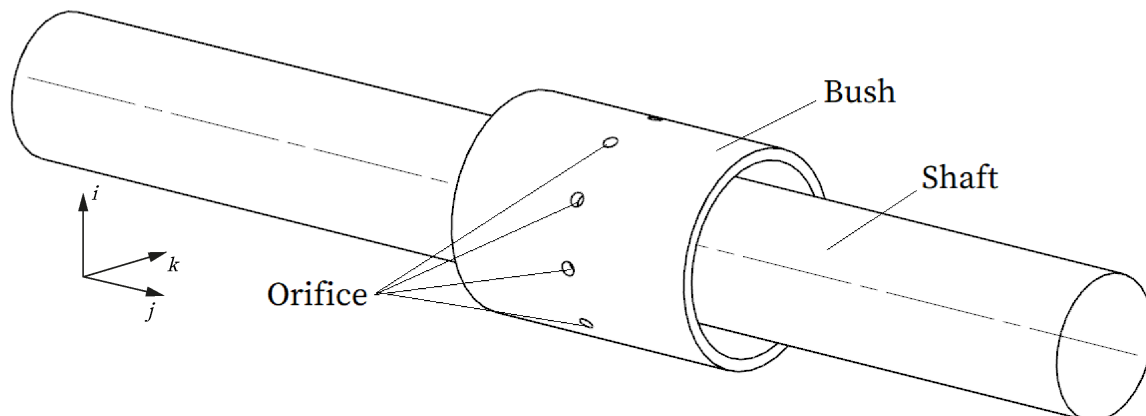
Figure 2.1. *Schematic layout of a journal air bearing. (Not to scale)*

2.1 Gas bearing geometry

The bearing under consideration is an industry case journal bearing. A journal bearing consists of a concentric cylindrical shaft and bush which move relative to each other in either the tangential or axial direction. In Figure 2.1 the layout of a journal air bearing is schematically illustrated in the system of Cartesian coordinates (i-j-k). Note that the distance between the shaft and the bush is exaggerated. The orifices are the supply holes through which the pressurized gas at constant supply pressure p_s flows radially inward to feed the air gap between the bush and the shaft. After the gas exits the orifice, the gas expands and exits the flow domain from the two outflow regions on either side of the bush. This constant flow of gas creates a thin fluid film between the bush and the shaft that generates the lubricating effect of a journal gas bearing. The bush can have one or multiple arrays of orifices in which the orifices are distributed evenly around the bush. The illustration above has only one array of orifices and this set-up will also be used in the remainder of this thesis.

2.1.1 Compensation

In case the shaft is located exactly centrally within the bush, the film height is equal along and around the bearing surface. This equilibrium height is known as the initial bearing clearance c and has a typical value in the order of microns. Assuming a perfect bearing surface and equal orifice geometries, the resistance to air flow through each orifice is equal. This results in a symmetric film pressure distribution and hence the net force on the shaft is zero.

The application of a radial load on the shaft displaces the shaft radially in the direction of the load, resulting in a film height that varies with angular position around the bush. This eccentric configuration for both the i-j and i-k cross sections of the journal bearing are illustrated in respectively Figure 2.2a and 2.2b. All important bearing parameters used for the model are aditionally illustrated. This eccentric configuration of the shaft within the bush increases the resistance to air flow through the orifices where the film height is decreased. Conversely, the resistance to air flow through the orifices on the side where the film height is increased in turn decreases. This difference in flow resistance results in a non-zero pressure differential between these two opposed areas and hence a non-zero net force on the shaft is induced. This phenomenon is referred to as compensation and is the mechanism that provides a journal gas bearing its stiffness. Given that the applied load W lies within the design limits of the bearing, an equilibrium is reached where the integrated pressure distribution is equal to the applied load.

(a) i-j plane   **(b)** i-k plane
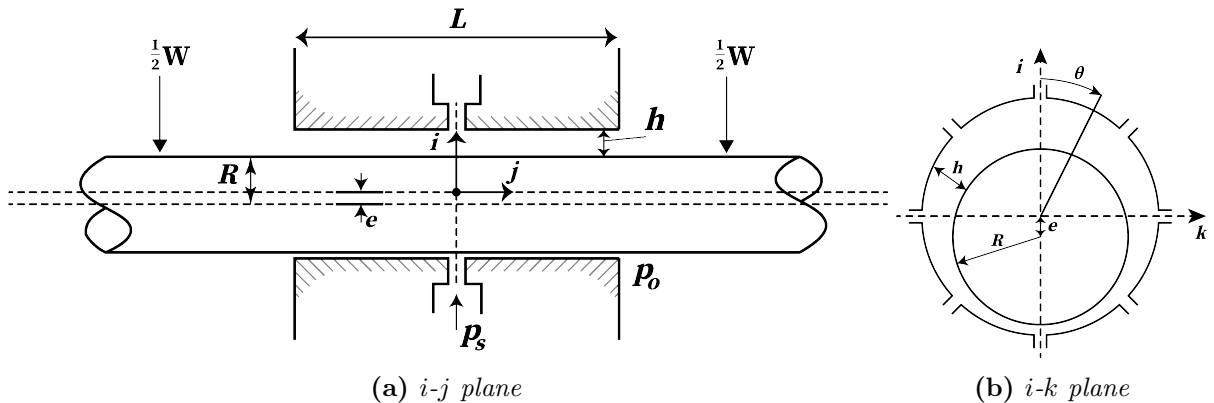
Figure 2.2. *Schematic representation of both the x-y (left) and x-z (right) cross sections of a loaded journal air bearing with radial displacement e. (Not to scale)*

The dimensionless eccentricity ratio ε is introduced to define a measure for the deviation to the concentric case. The eccentricity scales the radial displacement e to the bearing clearance as $\varepsilon = e/c$.

2.1.2 Thin film approximation

Given typical values for c and R used in this thesis as $10^{-6} \le c \le 50 \times 10^{-6}\ m$ and $R \ge 0.02$ m respectively, there exists a discrepancy in length scales between these bearing dimensions as $c \ll R$. This allows one to neglect the curvature of the fluid film in the journal bearing and map the 3-D cylindrical fluid domain depicted in Figure 2.1 to a 2-D rectangular domain [10]. This establishes a more simplistic description that benefits the meshing and post processing procedures as will be discussed in Chapter 3. In Figure 2.3, this mapped domain is schematically illustrated which will be used for in the remainder of this thesis. A total domain $\Omega \subset \mathbb{R}^2$ is considered which is constructed from the fluid domain Ω^f and the encapsulated orifice domain Ω^{or} as $\Omega = \overline{\Omega^f \cup \Omega^{or}}$. The y-axis coincides with the j-axis of Figures 2.1 and 2.2a and represents the length of the bearing. The x coordinate represents the circumferential position around the bearing as $x = \theta R$, with the circumferential angle θ in radians as illustrated in Figure 2.2b. The film height h is now parameterized and defined on every point on Ω along the z direction pointing towards the reader. Assuming the shaft only deflects vertically (no tilt), h can be described for $0 \le \varepsilon < 1$ as:

$$h(\theta) = c\left(1 + \varepsilon cos\left(\theta\right)\right) \tag{2.1}$$

Remark 2.1.1. *To elucidate this notation, the height field is in fact a map from the domain Ω to the set of real numbers as:*

$$h : \Omega \to \mathbb{R} \tag{2.2}$$

This means that h denotes the map, whereas $h(\vec{x}) = h(\theta)$ represents the point value of this map at angle θ.
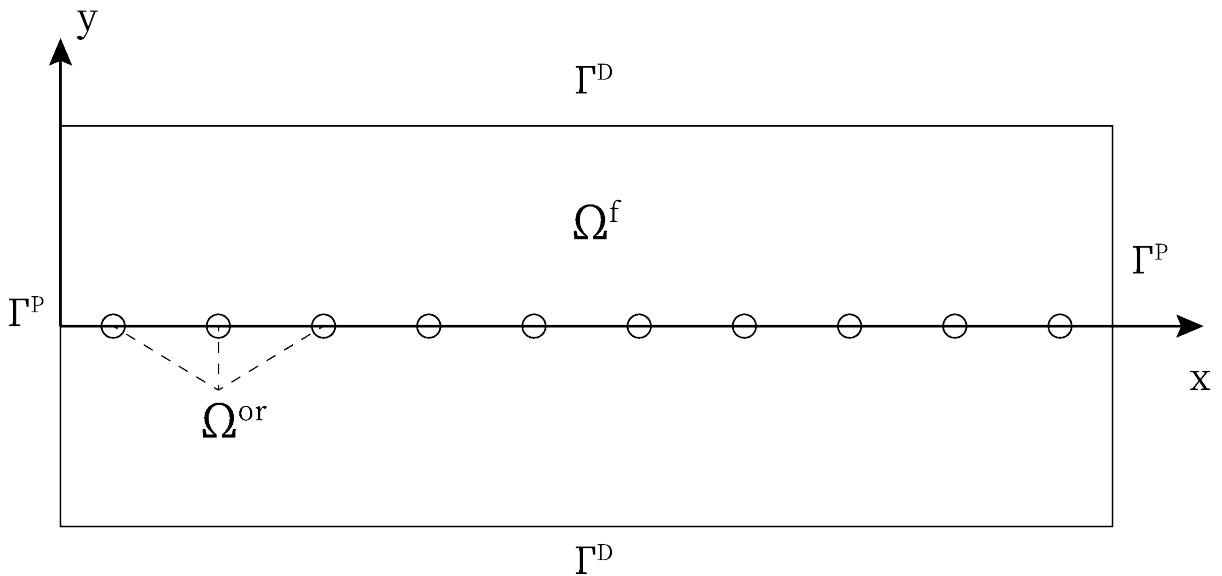
Figure 2.3. *Illustration of the rectangular fluid domain Ω^f with the encapsulated orifice domain Ω^{or} and boundaries Γ^D and Γ^P of the full air bearing geometry. (Not to scale)*

2.2 Mathematical description

With the geometry and the working principle of a journal gas bearing discussed, a mathematical model of such a bearing can be introduced. The thin gas film between the bush and the shaft can be described by a fully compressible viscous gas that agrees to the widely used Navier-Stokes equations. This set of equations consists of the conservation laws of mass (continuity) and momentum. Neglecting all body forces, these equations are given by respectively Equation (2.3) and (2.4) in Cartesian coordinates.

$$\frac{\partial \rho}{\partial t} + \nabla \cdot (\rho \vec{u}) = q \tag{2.3}$$

$$\frac{\partial (\rho \vec{u})}{\partial t} + \nabla \cdot (\rho \vec{u}) \vec{u} = -\nabla p + \nabla \boldsymbol{\sigma}^T \tag{2.4}$$

With density ρ, velocity vector $\vec{u}$, pressure p and stress tensor $\boldsymbol{\sigma}$. To incorporate the inflow through the orifice, the source term q is added to the continuity equation. This source term depicts the generation of mass per unit volume per unit time for each orifice and will later be elaborated further.

Remark 2.2.1. *Because of the fact that the viscosity of a gas is very small, the energy dissipated through the gas is negligible and hence the flow can assumed to be isothermal [11]. This removes the necessity of an energy equation.*

2.2.1 Reynolds equation

Taking into account the physical properties of the gas and the boundary conditions of the film, the mass and momentum equations may assume the form of the Reynolds equation. The Reynolds equation is a partial differential equation that describes a pressure distribution in a bearing gap and lies at the very foundation of lubrication theory, as it was first introduced for incompressible lubricants by Osborne Reynolds in 1886. Later Harrison (1913) incorporated the effects of compressibility. Looking at the case of a journal gas bearing, several assumptions can be made to arrive at the Reynolds equation which are listed below:

1. Any body forces acting on the entire system are neglected, including gravity, inertial accelerations and electric field accelerations.

2. Considering Remark 2.2.1, $c \ll \{R, L\}$ and hence the pressure gradient over the film height is negligible.

3. A Newtonian fluid is assumed, i.e. the shear stress changes linearly with the strain rate:

$$\boldsymbol{\sigma} = \mu \dot{\boldsymbol{\gamma}}$$

   Where $\dot{\boldsymbol{\gamma}} = \frac{1}{2} \left\{ \nabla \vec{u} + (\nabla \vec{u})^T \right\}$ the strain rate tensor. While no real fluid or gas fits the definition of a Newtonian fluid perfectly, common gases, such as air, do behave like one [12].

4. No slip boundaries on both the shaft and the bush.

5. Isoviscous flow. Fortunately the viscosity of gas is comparatively insensitive to changes in temperature and pressure and hence isoviscosity can be assumed [13].

6. Isothermal flow.

7. Laminar flow.

All assumptions are either evident or discussed above, except for assumption 7. Although it is showed in [14] that in typical hydrodynamically lubricated bearings the viscous forces are much greater than the inertial forces, one cannot assure laminar flow for all cases of bearing dimensions and boundary conditions. Given the small length scales of the film height and orifice diameter and the above mentioned viscous dominated flow, it is reasonable to assume laminar flow. Nonetheless, one should keep in mind that the validity of this assumption is bounded in the case of a journal gas bearing.

Taking these assumptions into account, the Reynolds equation can be derived by integrating the continuity equation across the film thickness and incorporating the momentum conservation onto which the no-slip boundary conditions are applied. This derivation is thoroughly elaborated in [14] and [15]. The resulting equation can be written as:

$$\nabla \cdot \left(\frac{h^3 \rho}{12\mu} \nabla p \right) - \frac{1}{2} \vec{u} \cdot \nabla (\rho h) + \int_0^h q \, \mathrm{d}z = \frac{\partial (\rho h)}{\partial t} \tag{2.5}$$

This equation is the most general form of the Reynolds equation and describes the pressure p on every point in the fluid domain between two surfaces separated by a small distance h. The relative velocity of the shaft to the bush is vectorised as $\vec{u} = \{u, v\}$ with relative horizontal and rotational velocities u and v respectively.

2.2.2 Physical significance of terms

To understand the mechanisms of how pressure can build up within a thin film, the different terms and their physical significance will be explored. Considering a one dimensional system with no sources, Equation (2.8) can be simplified yielding Equation (2.6).

$$\underbrace{\frac{\partial}{\partial x} \left(\frac{\rho h^3}{12\eta} \frac{\partial p}{\partial x} \right)}_{\text{Poiseuille flow}} - \underbrace{\frac{\partial}{\partial x} \left(\frac{\rho h \left(u_a \right)}{2} \right)}_{\text{Couette flow}} = \underbrace{\left(\frac{\partial (\rho h)}{\partial t} \right)}_{\text{Dynamic effect}} \tag{2.6}$$

$$\underbrace{\frac{h \left(u_a \right)}{2} \frac{\partial \rho}{\partial x}}_{\text{Density wedge}} + \underbrace{\frac{\rho h}{2} \frac{\partial}{\partial x} \left(u_a \right)}_{\text{Stretch}} + \underbrace{\frac{\rho \left(u_a \right)}{2} \frac{\partial h}{\partial x}}_{\text{Physical wedge}}$$

The tree main terms in the above equation are labeled as the Poiseuille flow, Couette flow and dynamic effects. Each have their own mechanism of pressure generation within the thin film and will be discussed below [14].

Poiseuille flow: Describes the net flow rates due to pressure gradients.

Couette flow: Describes the net flow rates due to surface velocities. Looking at its partial expansion to x, three distinct terms arise.

- The density wedge term is coupled to the rate at which the lubricant density changes in the sliding direction. This change in density is mostly temperature induced and hence not important as isothermal flow is assumed.

- The stretch term considers the rate at which the surface velocity changes in the sliding direction, e.g. a surface deformation. This mechanism is not encountered in this report as the bearing and the shaft are assumed to be rigid.

- The physical wedge term is the most important mechanism for pressure generation. This mechanism considers how a non-constant h field generates a flow. In the case h varies around the bearing ($\varepsilon > 0$), there is a different Couette flow rate at each point around the bearing. In order to still achieve continuity, a balancing Poiseuille flow is superimposed. Hence to generate a positive load carrying capacity, a non-zero eccentricity is required.

Dynamic effect: Describes the net flow rate due to dynamic effects. This can be split up into two mechanisms, namely a squeeze term and a local expansion term. The squeeze term generates a flow by considering the rate of change of h in time. The local expansion term generates a flow by a varying density in time.

2.2.3 Reynolds equation for compressible lubricants

Because of the fact that a compressible lubricant is considered, the density in Equation (2.5) is dependent on the pressure. lubricant density can therefore not be considered constant and hence an additional equation is required. By assuming the lubricant as an ideal gas, a pressure/density relation can be found in the equation of state given by Equation (2.7).

$$\rho = \frac{p}{R_s T_s} \tag{2.7}$$

Where T_s is the temperature of the supply gas and R_s is the specific gas constant defined as $R_s = \mathcal{R}/M$, with universal gas constant $\mathcal{R}$ and the molar mass of the considered gas M. By taking into account assumptions 5 and 6, Equation (2.5) can be written in its compressible form as:

$$\nabla \cdot \left(h^3 p \nabla p \right) - 6\mu \vec{u} \cdot \nabla \left(p h \right) + 12 \mu R_s T_s \int_0^h q \, \mathrm{d}z = 12\mu \frac{\partial \left(p h \right)}{\partial t} \tag{2.8}$$

2.2.4 Entrance flow model

As stated before, the inclusion of the continuous gas flow through the orifices is achieved through the source term q in Equation (2.3). This source term only applies to the encapsulated domain Ω^{or} and represents the mass flow per unit volume. This domain can either be modelled as a point source or as a sub area through which the mass flows. A point source has the advantage that it allows the usage of structured meshes and is computationally less expensive. Thererfore this modeling approach is chosen which allows to rewrite q in terms of the dirac delta function δ as:

$$q = \sum_{j=1}^{N} \dot{m}_j \delta^3 \left(\vec{x}_j^{or} \right) \tag{2.9}$$

With the mass flow rate through the jth orifice $\dot{m}_j$, the total number of orifices N and the location of the jth orifice $\vec{x}_j^{or} = \{x_j^{or}, y_j^{or}, z_j^{or}\}$. Since the Dirac delta has the inverse dimension as its argument, it can be seen that this expansion of q has the same dimension as q itself and is therefore dimensionally valid. The definition of the Dirac delta function is given by Equation (2.10).

$$\delta^3 \left(\vec{x}_j^{or} \right) \triangleq \delta \left(x - x_j^{or} \right) \delta \left(y - y_j^{or} \right) \delta \left(z - z_j^{or} \right) \tag{2.10}$$

With the identity for all sufficiently smooth function ϕ as:

$$\iiint_\Omega \delta^3 \left(\vec{x} - \vec{x_j^{or}} \right) \phi(\vec{x}) \mathrm{d}V = \phi(\vec{x}_j^{or}) \tag{2.11}$$

In literature, several types of orifices exists which each require a different modelling approach [13, 16]. The two most used in industry are the inherently compensated orifice and the pocketed compensated orifice. The inherently compensated type is practically a small hole drilled into the surface of the bush. A pocketed compensated orifice is machined by recessing the area around the orifice to allow for a larger area where the pressure is equal to the downstream pressure of the orifice. These pocketed compensated orifices typically have a greater stiffness by a factor of up to 1.5 [16]. Because of their relative simplicity, only inherently compensated orifice restrictors are considered in this thesis.

Inherent compensation

In Figure 2.4 an enlarged geometry of an inherently compensated orifice restrictor is illustrated with the corresponding pressure profile. As can be seen in this figure, the entrance flow from supply pressure to film entrance pressure is described by the actual pressure profile. After recovery this actual pressure profile is dominated by viscous flow. In literature, methods are proposed to solve for this actual pressure profile [17]. However, a more practical approach would be to formulate a lumped-parameter approach to account for the entrance effects without the necessity to solve for the actual pressure profile for each given bearing configuration. This is achieved by relating the mass flow rate to the pressure ratio $\beta = p_t/p_s$. Where p_t is the theoretical static downstream orifice pressure which is obtained by extrapolating the viscous profile in the film [18]. Given that the dimensions of an orifice are very small compared to the other bearing dimensions, the expansion of the gas through the orifice curtain area occurs extremely fast and this process can therefore be assumed isentropic. An expression for the mass flow rate through the jth orifice can be found by using the isentropic relations yielding Equation (2.12).

$$\dot{m}_j = C_D A_{or,j} \frac{p_s}{\sqrt{T_s R_s}} \Psi(p_t) \tag{2.12}$$

With the area of the jth orifice $A_{or,j}$ and lubricant supply temperature T_s. C_D is the coefficient of discharge that depends on the orifice geometry and is typically taken to be 0.8 in literature [19]. As β decreases, the mass flow through the orifices increases up until the point the critical pressure ratio β_γ reached. At this point the flow is choked and has reached its maximum velocity, any further downstream pressure reduction cannot increase the flow rate. The flow function Ψ
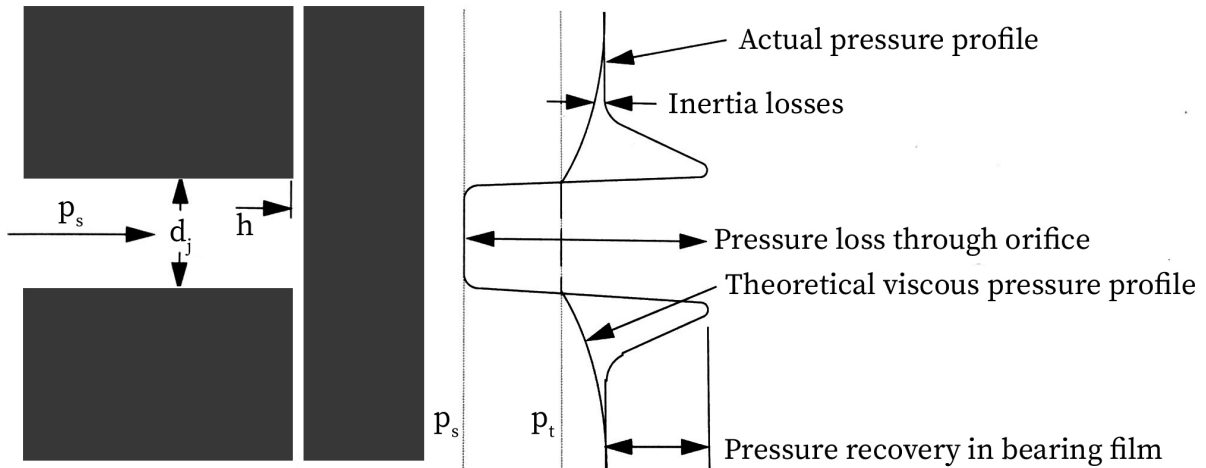
Figure 2.4. *Local pressure losses in an inherently compensated orifice restrictor [16].*

assures the mass flow through an orifice is bounded according to Equation 2.13. For an isentropic gas flow the critical pressure β_γ is given by Equation 2.14.

$$\Psi(p_t) = \begin{cases} \sqrt{\left(\frac{2\gamma}{\gamma-1}\right)\left(\frac{p_t}{p_s}^{2/\gamma} - \frac{p_t}{p_s}^{\gamma+1/\gamma}\right)} & \text{if } p_t/p_s \geq \beta_\gamma \\ \sqrt{\left(\frac{2\gamma}{\gamma-1}\right)\left(\beta_\gamma^{2/\gamma} - \beta_\gamma^{\gamma+1/\gamma}\right)} & \text{if } p_t/p_s \leq \beta_\gamma \end{cases} \tag{2.13}$$

$$\beta_\gamma = \left(\frac{2}{\gamma+1}\right)^{\frac{\gamma}{\gamma-1}} \tag{2.14}$$

2.2.5 Boundary and initial conditions

The considered domain is supplemented with Dirichlet and periodic boundary conditions on complementary parts of the boundary $\partial\Omega$. For the Dirichlet (Γ^D) and the periodic (Γ^P) boundaries it holds that $\overline{\Gamma^D \cup \Gamma^P} = \Gamma = \partial\Omega$. The periodic boundaries assure that the left and right sides of the domain coincide by letting $\phi_x|_{\theta=0} = \phi_x|_{\theta=2\pi}$ with smooth real functions $\phi : \mathbb{R}^2 \to \mathbb{R}$. The Dirichlet boundaries define the outflow pressure of the gas. When symmetry axes are defined, as will later be discussed in Chapter 3, the periodic boundaries are replaced with Neumann boundaries Γ^N. On these boundaries the normal pressure gradient is described as $\vec{n} \cdot \nabla p = 0$.

The initial conditions are defined as the pressure field at $t = 0$. This can either be the static solution of the concentric or eccentric configuration defined by ε.

2.3 Dimensionless Reynolds equation

Often it is convenient to write Equation (2.8) in dimensionless form by means of normalization. Introducing a set of dimensionless variables and parameters, let

$$x = R\tilde{x}, \quad y = R\tilde{y}, \quad p = p_a\tilde{p}, \quad h = c\tilde{h}, \quad t = t_a\tau, \quad \nabla = \frac{1}{R}\tilde{\nabla} \tag{2.15}$$

where p_a and t_a are the characteristic pressure and time constants. Typically these are set to be the ambient pressure and a characteristic frequency, respectively. In this case the characteristic time is proportional to the induced horizontal shaft velocity as $t_a = \frac{u_u}{L}$. The dimensionless gradient operator is defined as $\tilde{\nabla} = \left\{\frac{\partial}{\partial\tilde{x}}, \frac{\partial}{\partial\tilde{y}}\right\}$. The dimensionless outflow pressure at the Dirichlet boundaries is rewritten accordingly as $p_o = p_a\tilde{p}_o$. Incorporating above definitions into Equation 2.8 and assuming inherent compensation as discussed above, the Reynolds equation in its dimensionless form is written as:

$$\tilde{\nabla} \cdot \left(\tilde{h}^3\tilde{p}\tilde{\nabla}\tilde{p}\right) - \vec{\Lambda} \cdot \tilde{\nabla}\left(\tilde{p}\tilde{h}\right) + \sum_{j=1}^{N} \Upsilon\dot{m}_j(\tilde{p})\delta^2(\vec{x}_j^{or}) = \Pi\frac{\partial}{\partial\tau}\left(\tilde{p}\tilde{h}\right) \tag{2.16}$$

where:

$$\vec{\Lambda} = \frac{6\mu R}{c^2 p_a}\vec{u}$$
$$\Upsilon = \frac{12\mu R_s T_s R^2}{c^3 p_a^2} \tag{2.17}$$
$$\Pi = \frac{12\mu R^2 L}{c^2 p_a u_u}$$

are known as the bearing number, the feeding parameter and the frequency or squeeze number respectively [20]. Note that the bearing number is vectorised as $\vec{\Lambda} = \{\Lambda_u, \Lambda_v\}$. The resulting dimensionless partial differential equation is clearly elliptic and nonlinear. This is due to the divergence of the pressure gradient in the poiseuille term and the coupled mass flow equation in the source term. Nonlinear solution methods are therefore required to solve this problem as will be discussed in the next chapter. Note that negative pressures are not excluded by the above equation. Negative pressures would mean a physically infeasible solution and should be excluded through the selection of proper boundary conditions.

2.4 Problem definition

Combining the geometry and the mathematical formulation of the Reynolds equation of previous sections, a problem definition can be constructed in both the strong and weak form. Looking at the domain as proposed in section 2.1.2, two symmetry axes can be recognized. As in the remainder of this thesis only horizontal shaft velocities will be induced ($\Lambda_v = 0$), a vertical symmetry axis arises which reduces the horizontal axis to ($0 \leq \theta \leq \pi$). This allows one to only model half an air bearing, reducing the computational cost of the numerical calculations. It is important to note that in this case the periodic boundary conditions Γ^P in Figure 2.3 must be replaced with Neumann boundary conditions Γ^N prescribing the normal pressure gradient at these boundaries.

2.4.1 Strong formulation

Considering the domain Ω with supplemented boundary $\overline{\Gamma^D \cup \Gamma^N} = \Gamma = \partial\Omega$, the pressure distribution as a result of a shaft deflection ε is described by the strong form problem ($\mathcal{S}$) as:

$$(\mathcal{S}) \begin{cases} \text{Given } h : \Omega \to \mathbb{R}^2 \text{ and constants } \Lambda, \Upsilon \text{ and } \Pi, \\ \text{find } p : \Omega \to \mathbb{R}^2 \text{ such that:} \\ \nabla \cdot \left(h^3 p \nabla p \right) - \vec{\Lambda} \cdot \nabla \left(ph \right) + \sum_{j=1}^{N} \Upsilon \dot{m}_j(p) \delta^2(\vec{x}_j^{or}) = \Pi \frac{\partial}{\partial \tau} \left(ph \right) & \text{in } \Omega \\ n \cdot \nabla p = 0 & \text{on } \Gamma^N \\ p = p_a & \text{on } \Gamma^D \end{cases} \quad (2.18)$$

2.4.2 Weak formulation

The finite element method that will be used in this thesis is generally used in conjunction with the weak form of the problem. The weak form is obtained by the multiplication of the differential equation 2.8 by an arbitrary test function and integrating it over its domain Ω. To arrive at the weak form of 2.18, the suitable scalar-valued Sobolev spaces $\mathcal{V}$ and $\mathcal{S}$ are introduced that make up the test and trial spaces respectively according to Equation 2.19 and 2.20.

$$\mathcal{V} = \left\{ \varphi \mid \varphi \in H^1(\Omega), \varphi = 0 \text{ on } \Gamma^D \right\} \quad (2.19)$$

$$\mathcal{S} = \left\{ p \mid p \in H^1(\Omega), p = p_a \text{ on } \Gamma^D \right\} \quad (2.20)$$

Note that the trial functions meet the Dirichlet condition and the test functions vanishes at the Dirichlet boundaries. Using these spaces, the problem definition can be described in its weak formulation as:

$$(\mathcal{W}) \begin{cases} \text{Given } h : \Omega \to \mathbb{R}^2 \text{ and constants } \Lambda, \Upsilon \text{ and } \Pi, \\ \text{find } p \in \mathcal{S} \text{ such that:} \\ \mathcal{B}(\varphi, p) + \mathcal{M}(\varphi, p) = \mathcal{F}(\varphi) \quad \forall \varphi \in \mathcal{V} \\ \text{where:} \\ \mathcal{B}(\varphi, p) = \int_\Omega (\nabla \varphi) \cdot \left(h^3 p \nabla p - 2hp\vec{\Lambda} \right) \mathrm{d}V \\ \mathcal{M}(\varphi, p) = -\dfrac{\partial}{\partial \tau} \int_\Omega \varphi \left(\Pi p h \right) \mathrm{d}V \\ \mathcal{F}(\varphi) = \sum\limits_{j=1}^{N} \int_{\Omega^{or}} \varphi \left(\Upsilon \dot{m}_j(p_t) \delta^2 (x_j^{or}) \right) \mathrm{d}V = \sum\limits_{j=1}^{N} \varphi(\vec{x}_j^{or}) \left(\Upsilon \dot{m}_j (p_t(\vec{x}_j^{or})) \right) \end{cases} \qquad (2.21)$$

Chapter 3

Numerical simulations

While different numerical strategies for solving mathematical models such as the one presented in Chapter 2 exist, only the finite element method (FEM) is considered throughout this thesis. Although FEM is not the industry standard for computational fluid dynamics, its accuracy with respect to solving these elliptical partial differential equations on potentially complex domains allows for an accurate and modular model. In this chapter the implementation of the weak formulation (2.21) into a FEM framework is discussed. A convergence study is performed to determine the quality of the model and the validity of the obtained output. This model is then solved for different cases both stationary and transient. At last a validation of this predictive model is included by means of numerical and empirical analyses found in literature.

3.1 Discretization

Given the bilinear and linear form from the weak form as $\mathcal{B}(\varphi, p) + \mathcal{M}(\varphi, p)$ and $\mathcal{F}(\varphi)$ respectively, a discrete model can be constructed by applying the Bubnov-Galerkin method. Therefore the infinite dimensional trial and test spaces $\mathcal{S}$ and $\mathcal{V}$ are approximated by their discrete and finite dimensional counterparts, in terms of the discrete test space $\mathcal{V}^h$ according to Equation (3.1). The superscript h indicates the space is finite dimensional.

$$\mathcal{S}^h = \left\{ v^h + q^h \mid v^h \in \mathcal{V}^h \right\} \tag{3.1}$$

With q^h a lifting function that satisfies the boundary conditions. The weak problem (2.21) can be written in its finite dimensional form $(\mathcal{G})$ as:

$$(\mathcal{G}) \begin{cases} \text{Find } v^h \in \mathcal{V}^h \text{ such that:} \\ \mathcal{B}(\varphi^h, v^h) + \mathcal{M}(\varphi^h, v^h) = \mathcal{F}(\varphi^h) \quad \forall \, \varphi^h \in \mathcal{V}^h \end{cases} \tag{3.2}$$

A finite element mesh is constructed in order to discretise the domain Ω. Two mesh types are considered, a structured mesh using quadrilateral elements and an unstructured mesh using triangular elements. The fact that point sources are used to model the orifices allows one to apply the former type. This has the additional advantages of higher computational efficiency, easier meshing procedures and better convergence propperties. In Figure 3.1 an example of a uniform and structured mesh with quadrilateral elements is illustrated, the location of the nodal point sources is marked in red. A mesh refinement is achieved by cutting the element in half in both directions. Formally speaking, the level of mesh refinement is controlled through the element width h which is defined as $h = h_0/2^n$, where h_0 is the minimal element width and $n = 0, 1, 2, ..$ a refinement factor. Note that the aspect ratio of the elements remains the same for each refinement.

Table 3.1. *Default bearing dimensions and flow parameters used for the numerical simulations. For the gas lubricant air will be used.*

Parameters	Values
Shaft radius (R)	$22.5\ mm$
Bush length (L)	$50\ mm$
Bearing clearance (c)	$13\ \mu m$
Orifice radius (d)	$10\ \mu m$
Number of orifice rows	1
Number of orifices per row (N)	10
Outflow pressure (p_o)	$1.0 \times 10^5\ Pa$
Supply pressure (p_s)	$6.0 \times 10^5\ Pa$
Atmospheric pressure (p_a)	$1.0 \times 10^5\ Pa$
Air temperature (T_s)	$293\ K$
Air dynamic viscosity (μ)	$1.79 \times 10^{-5}\ Pa \cdot s$

For all the conducted simulations the free and open source Python programming library for FEM computations *Nutils* is used [21]. Quadratic spline basis functions are used, which on a structured mesh with $n = 0$ results in approximately 120 degrees of freedom. An iterative Newton-Raphson method is used to solve the non-linear partial differential equation, using a uniform pressure field of value p_o as an initial guess. The allowed absolute tolerance of the residual norm is set at 10^{-10}. Unless stated differently, the default flow conditions and bearing dimensions as listed in Table 3.1 are used for the numerical simulations conducted in this chapter.

3.2 Steady state results

The static solution to $(\mathcal{G})$ is computed for an increasing value of ε. An example of the film height $h(x, y)$, which is used as an input to the model, is illustrated in Figure 3.2 for $\varepsilon = 0.5$. Figure 3.3 then shows the computed static solutions for eccentricy values $\varepsilon = 0.0, 0.2, 0.4$ and 0.6 using $n = 2$ and $\Lambda_u = 0$. It can be seen that the solution of the concentric case shows a symmetric pressure profile and a smooth pressure decay towards the outflow regions as one would expect. For $\varepsilon > 0.0$, the pressure drop over the orifices decreases where the film height increases, clearly demonstrating the compensation mechanism as discussed in Chapter 2.
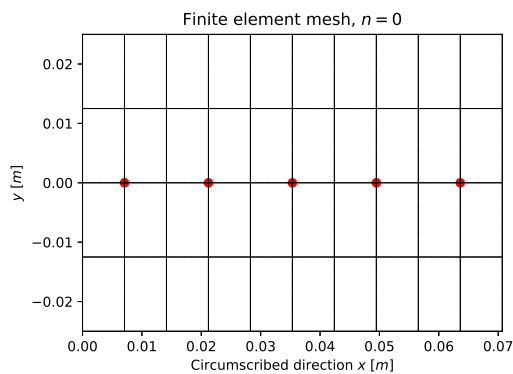
Figure 3.1. *Finite element mesh for $n = 0$.*
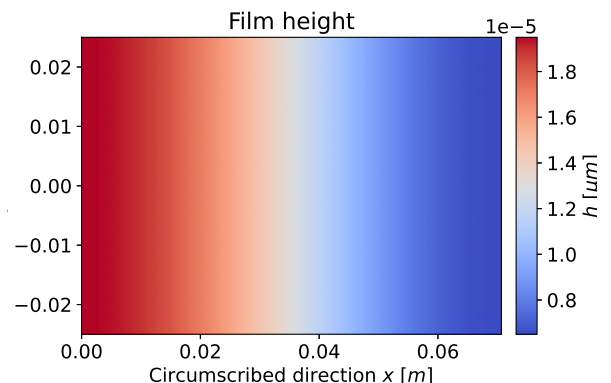
Figure 3.2. *Film height for $\varepsilon = 0.5$.*

(a) $\varepsilon = 0.0$

(b) $\varepsilon = 0.2$

(c) $\varepsilon = 0.4$

(d) $\varepsilon = 0.6$
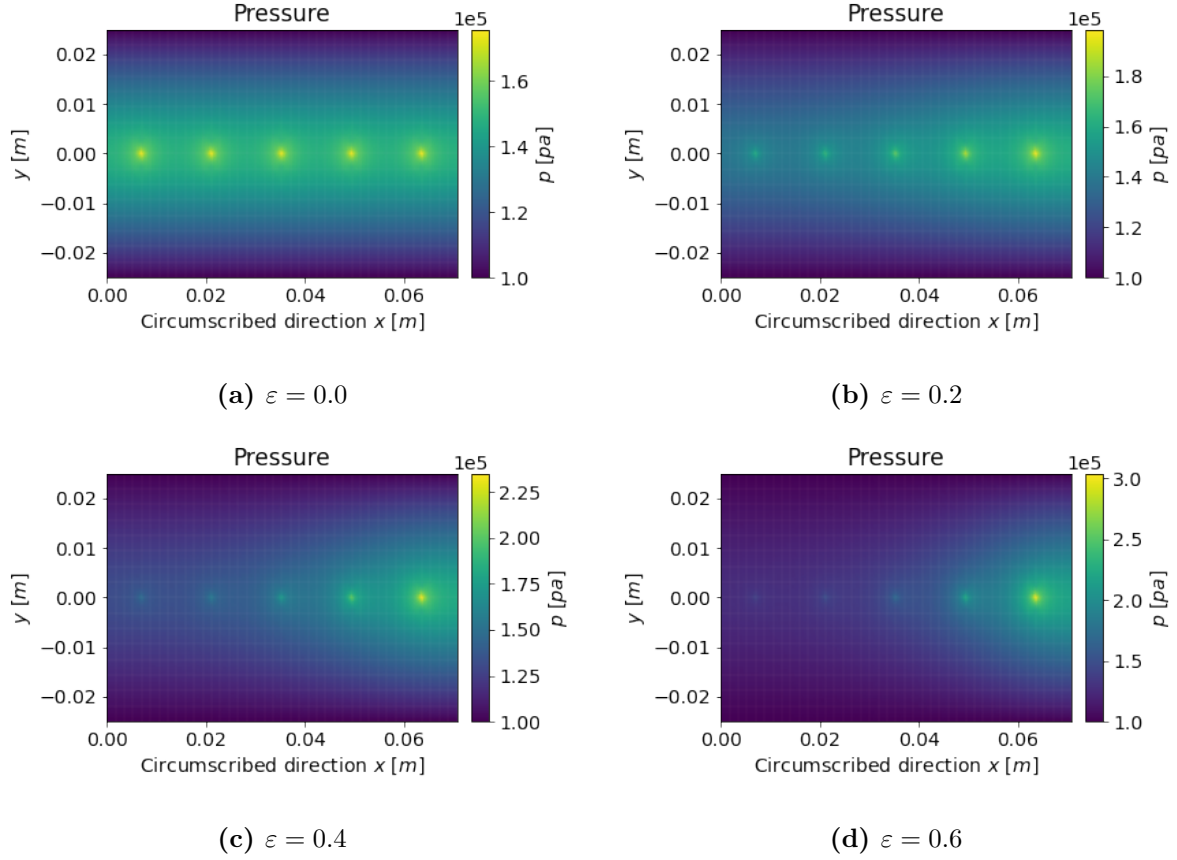
Figure 3.3. *Steady state pressure distribution for increasing eccentricities and* $\Lambda_u = 0$.

3.2.1 Static characteristics

The static stiffness of a gas bearing is calculated through the load capacity which is directly related to the pressure distribution of the thin gas film. Integrating the computed pressure distribution, the load capacity of the bearing is given according to Equation (3.3). Note that this represents the net force as there is compensated for the outflow pressure. The static stiffness is then obtained by the differential of the load capacity with respect to the film height, as given by Equation (3.4). As only vertical shaft deflections are considered, the horizontal component F_x will in all cases be zero and therefore only the vertical component F_y will be used.

$$\left\{ \begin{array}{c} F_x \\ F_y \end{array} \right\} = -2 \int_{-L/2}^{L/2} \int_{0}^{\pi} (p - p_o) \left\{ \begin{array}{c} \cos(\theta) \\ \sin(\theta) \end{array} \right\} R \, \mathrm{d}\theta \mathrm{d}y \tag{3.3}$$

$$K = -\frac{dF}{dh} = -\frac{dF}{d\varepsilon}\frac{d\varepsilon}{dh} = -\frac{1}{c}\frac{dF}{d\varepsilon} \tag{3.4}$$

Additionally, with the static pressure distribution the mass flow rate of gas can be computed. This expression is derived from the mass of gas flowing between two plates separated by a finite but small distance [19]. Integrating this expression over the Dirichlet boundaries, the mass flow over the outflow boundaries is defined according to Equation (3.5). A massflow residual function can then be defined as $\dot{m}_{in} - \dot{m}_{out} = 0$.

$$\dot{m}_{out} = \int_{\Gamma^D} \frac{p}{R_s T_s} \left(\frac{h^3}{12\mu}\nabla p + \frac{\vec{u}h}{2} \right) \cdot \vec{n} \, \mathrm{d}S \tag{3.5}$$

3.2.2 Convergence study

Mass flow

Given the definitions of the quantities of interest above, the mesh convergence of the air bearing model can be assessed. The above defined air bearing problem is solved for an increasing number of degrees of freedom, and for eccentricy values $\varepsilon = 0.0$, $\varepsilon = 0.2$ and $\varepsilon = 0.4$. In Figure 3.4 the effect of grid size to the mass residual error is reported on grids with $n = 0, 1, 2, 3, 4$ and 5, resulting in systems between approximately 120 and 11200 degrees of freedom. Figure 3.4a contains the convergence properties for $\Lambda_u = 0.0$. The convergence rate for each eccentricity has a slope of approximately 2.0. Figure 3.4b contains the convergence properties for $\Lambda_u = 1.0$, which shows very similar results to those using $\Lambda_u = 0.0$. However, the values of the relative mass residual are one order of magnitude higher compared to $\Lambda_u = 0.0$.

Load capacity

The load capacity is the quantity of interest (QOI) and directly relates to the stiffness of the bearing. Its convergence should therefore be studied carefully. As stated in Chapter 2, the load capacity in the concentric situation ($\varepsilon = 0$) should be zero. To validate this for an increasing number of degrees of freedom, the effect of the grid size to the load capacity at zero eccentricity is reported in Figure 3.5, for both zero and non-zero bearing numbers. The results show close to zero load capacities at almost machine precission in all cases for both bearing numbers.

The residual function of the load capacity is defined as $|F^h - F^e|$, where the superscript h defines an approximated solution for the load capacity and the superscript e the exact solution. Due to the absence of an analytical solution, the exact solution is assumed to be a FEM solution solved on a grid with $n = 6$, resulting in a system with approximately 42200 degrees of freedom. In Figure 3.6 the effect of grid size to the relative load capacity residual is reported on the same grids as used for the mass flow residual analysis. Figure 3.6a contains the convergence for $\Lambda_u = 0.0$ and Figure 3.6b for $\Lambda_u = 1.0$. The results are very similar to those of the mass flow residual, however, now with a slighly steeper convergence rate for $\Lambda_u = 1.0$.

From these results one could state that the solutions on a grid with $n = 2$ have acceptable results while still maintaining a workable mesh size in terms of computational time. Allowing a relative mass flow error of around 8×10^{-3}, and a relative error in load capacity of around 10^{-5}.

(a) $\Lambda_u = 0.0$ (b) $\Lambda_u = 1.0$
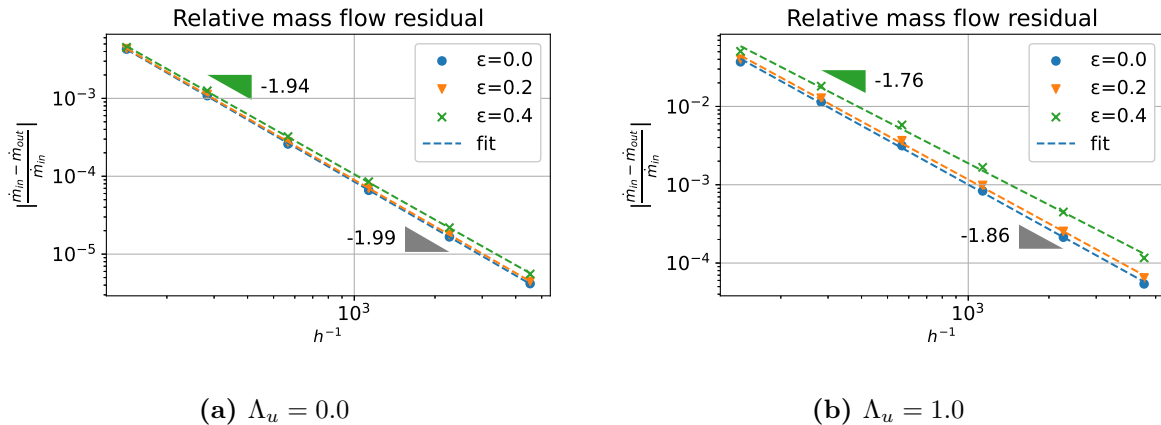
Figure 3.4. *Relative mass flow residual for $\Lambda_u = 0.0$ and $\Lambda_u = 1.0$*
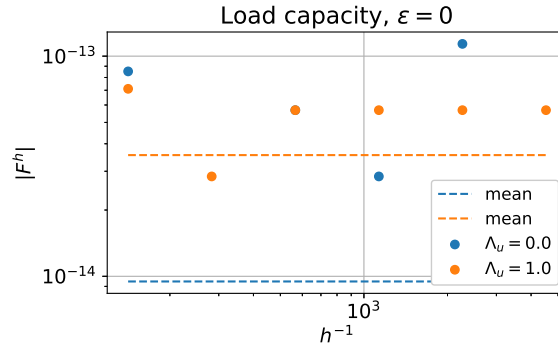
Figure 3.5. *Absolute load capacity at $\varepsilon = 0$ for both $\Lambda_u = 0.0$ and $\Lambda_u = 1.0$.*

(a) $\Lambda_u = 0.0$

(b) $\Lambda_u = 1.0$
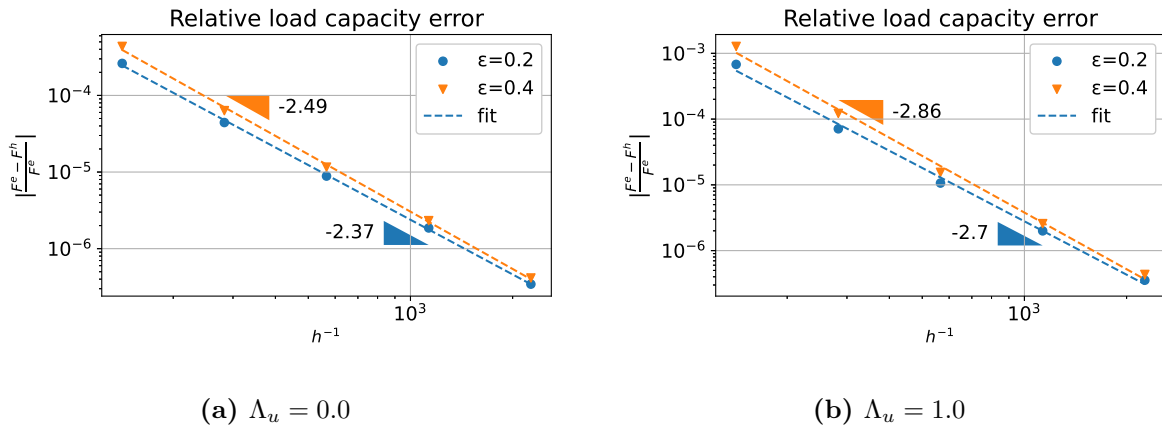
Figure 3.6. *Relative load capacity residual for $\Lambda_u = 0.0$ and $\Lambda_u = 1.0$*

Error norms

As an addition to the convergence of the QOI's, the convergence rates of the pressure solution in the normed space $\mathcal{V}$ are investigated. Figure 3.7 reports the convergence rates of both the $L^2(\Omega)$ and $H^1(\Omega)$ error norms of the solution with respect to the grid size. Considering the $H^1(\Omega)$ error norms, a quasi-optimal solution would have a convergence rate of $p + 1 - m = 2$ for $m = 1$. This means that the convergence rates shown in Figures 3.7b and 3.7d are suboptimal. This is due to the fact that the orifices in the domain are modeled as point sources around which great pressure gradients arise. The solution therefore exhibits singularies at the location of these point sources which causes the convergence rates to be sub-optimal. A condition number of the residual is found to be approximately 10^3. Adaptive mesh refinement around the orifices may increase the convergence rates and reach quasi-optimality. However, as the convergence of the integrated solution on uniform gridsd is already acceptable for both the mass flow residual and load capacity residual, adaptive mesh refinement is not investigated any further.

Remark 3.2.1. *It should be pointed out here that the contribution of the flow through the orifices to the pressure solution grows with increasing orifice diameter d. One could say that the analytical solution of the isentropic flow is effectively coupled through this parameter to the numerical solution in the remainder of the domain. It is observed that for increasing d the convergence becomes significantly poor, resulting in unacceptable values for the mass flow residual, load capacity residual and $L^2(\Omega)$ error norm. Adaptive mesh refinement for structured meshes*

(a) $\Lambda_u = 0.0$

(b) $\Lambda_u = 0.0$

(c) $\Lambda_u = 1.0$
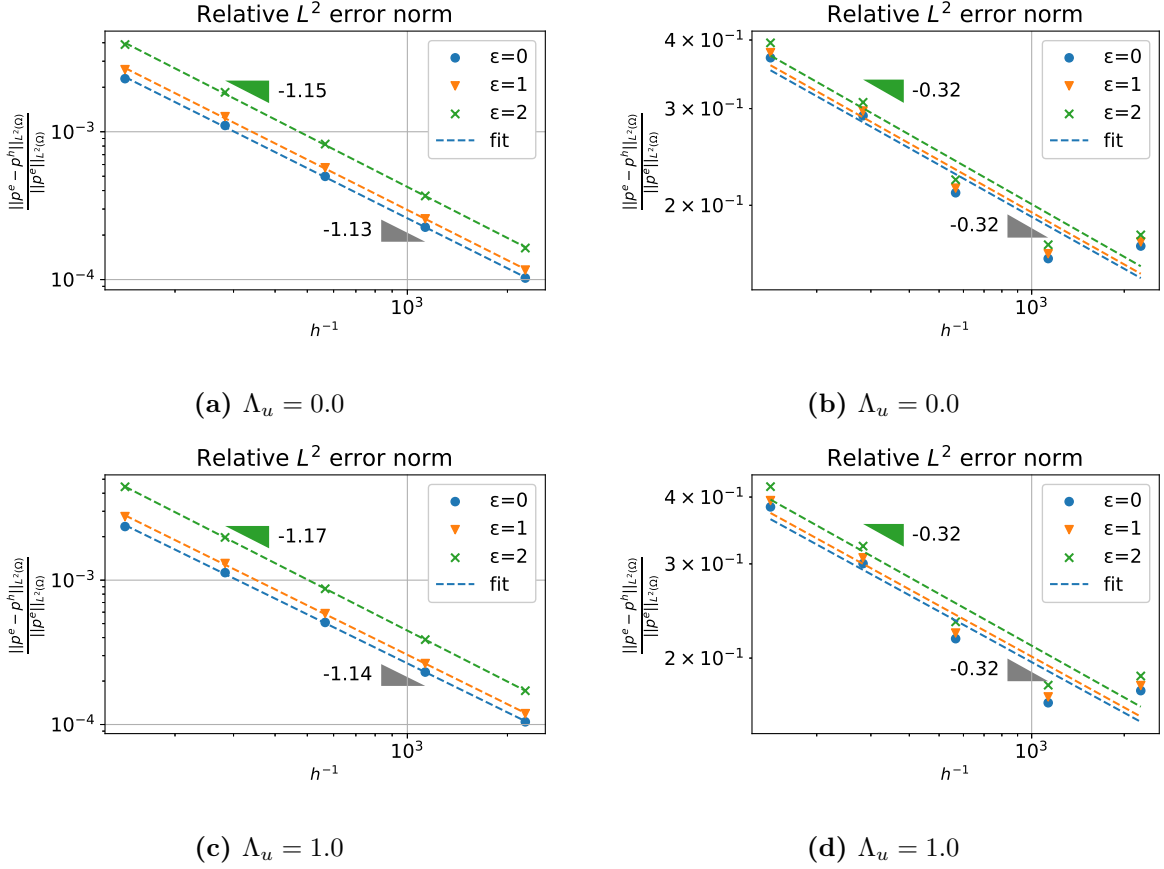
(d) $\Lambda_u = 1.0$

Figure 3.7. *Relative $L^2(\Omega)$ and $H^1(\Omega)$ error norms for increasing eccentricity at both $\Lambda_u = 0.0$ and $\Lambda_u = 1.0$.*

is therefore advised for higher values of d. Another alternative would be to model the orifices as finite areas using unstructured grids. The latter option is elaborated further in Appendix A, reporting results using this method. In the remainder of this thesis only stable values for d are used with uniform structured grids.

3.2.3 Parameter dependency

As the convergence behaviour of the numerical model shows promising and reliable results, the output of the model is compared to results in literature. Figure 3.8 reports both the static load capacity and stiffness characteristics as a function of eccentricity ratio according to Equations (3.3) and (3.4). The output at $\varepsilon = 0$ behaves as expected with a zero load capacity and a non-zero stiffness. For increasing values of ε, the load capacity and stiffness increase which is a direct result of the compensation mechanism. This confirms the observation in Chapter 2.2.1 that a non-zero eccentricity is required to generate a positive load capacity. Similar behaviour is also observed in literature which also confirms the order of magnitude of both the load capacity and stiffness [5, 12, 19, 20, 22, 23]. Alltough an exact qualitative comparison cannot be made, the static model does behave as expected with trustworthy results.

The effect of the initial bearing clearance to the static stiffness is reported in Figure 3.9. The static bearing stiffness is plotted for a range of bearing clearances and eccentricities. It clear that the bearing clearance has a great effect on the stiffness especially for $c \geq 4 \times 10^{-6}$. Here the stiffness increases significantly at low eccentricities for decreasing c, which is in correspondance

(a) *Vertical static load capacity*

(b) *Vertical static stiffness*
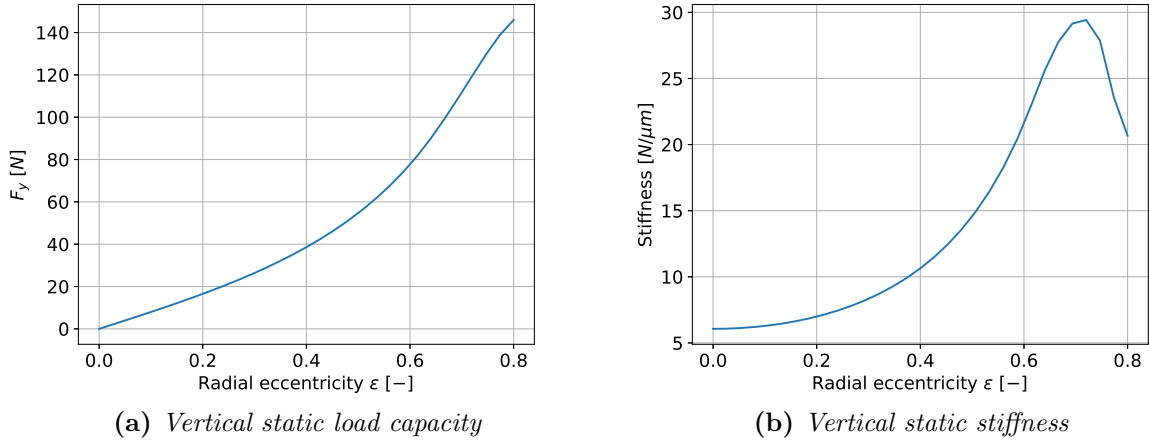
Figure 3.8. *Static bearing characteristics as a function of ε. The simulation is conducted for the default bearing geometry and parameters, $\Lambda_u = 0$.*
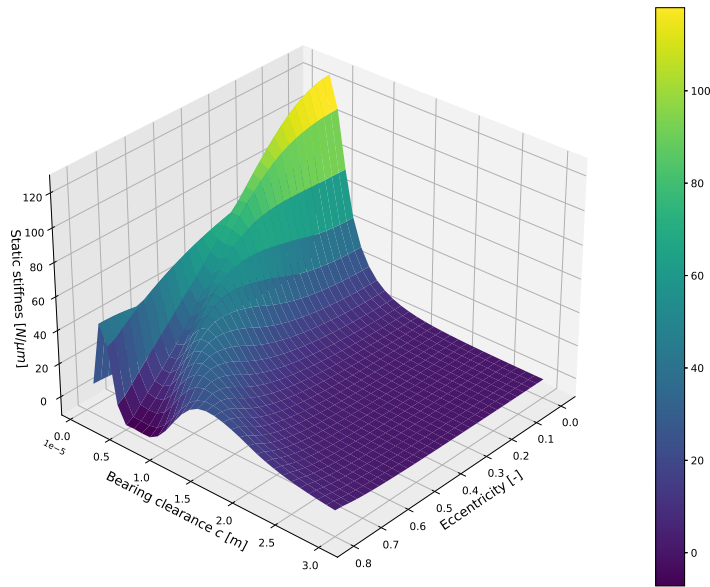
Figure 3.9. *Static stiffness as a function of h_0 and ε*

with theories found in literature [19]. It is good to note that this theory breaks down at the extreme configuration $10^{-6} \leq c < 3 \times 10^{-6}$. This is most likely due the fact that the pressure gradient over the shaft is small because the resistance to air flow through the orifice for these values of c is already relatively high at low eccentricity.

3.3 Transient results

To investigate the dynamic characteristics of the bearing model, a transient simulation is conducted. For this simulation the same spatial discretization is used as discussed in the previous section. For the time discretization an implicit Euler scheme is applied for which a steady state solution at $\varepsilon = 0.0$ is used as an initial condition. The dynamic response is visualized by evaluating the Reynolds equation at various excitation frequencies around the equilibrium

point at $t = 0$. For this, a sinusoidal pertubation is added to Equation (2.1) resulting in a time dependent film height as:

$$h(\theta, t) = \underbrace{h_0}_{1} + \underbrace{h_0 \varepsilon \cos(\theta)}_{2} + \underbrace{de \cos(\theta) \sin(\omega t)}_{3} \tag{3.6}$$

Where ω is the pertubation frequency of the shaft and de the amplitude of this pertubation. Typical values used for de lie within 10% of the initial bearing clearance. The three components from above definition may be interpreted as:

1. The initial bearing clearance as determined in the design of the bearing.

2. A manufacturing error or static load which results in an eccentric configuration quantified by ε.

3. The dynamic behaviour of the shaft.

To ensure the transient response is converged, the simulation is conducted up untill the difference in amplitude of the response of at least three complete and consecutive pertubation periods lie within 5%. The timestep of the simulation is set to be approximately 1/20th of the pertubation period to ensure the time dependent film height is properly discretised in time.

3.3.1 Dynamic characteristics

The dynamic bearing stiffness and damping characteristics can be determined by the evaluation of the transfer function H at a given frequency. For the above defined transient analysis this requires the computation of the magnitude and phase angle of the input/output response. In this analysis this information is obtained by transforming the time response to the frequency domain by means of a Fourier transform. The resulting complex valued transfer function H can then be used to compute the dynamic stiffness and damping characteristics according to Equation (3.7) and (3.8) respectively.

$$K = |H| \cos(\angle H) \tag{3.7}$$

$$C = \frac{|H|}{\omega} \sin(\angle H) \tag{3.8}$$

In Figure 3.10 the dynamic coefficients as a function of the pertubation frequency ω are reported in the form of a bode plot for both zero and non-zero eccentricities. Considering Figure 3.10a, frequency dependency of the dynamic coefficients is clearly observed, i.e., for increasing ω the dynamic stiffness significantly increases while the dynamic damping decreases. The relationship between the dynamic coefficients and ω is clearly non-linear which is due to the compressibility effects discussed in Section 2.2.2. For the lower frequency range below approximately 1 Hz, the stiffness is asymptotically equal to the static stiffness depicted in Figure 3.8b. For higher frequencies the dynamic squeeze film becomes dominant and the dynamic stiffness increases significantly with increasing ω. In the high frequent range above approximately 10 kHz an asymptotic value is reached. The dynamic damping response behaves very similar but inverted, with a larger damping value in the lower frequency range, and becomes negligible beyond 1 kHz. Very similar results are also found in literature, which strenghtens these observations [5, 24, 25].

The results for the eccentric case depicted in Figure 3.10b are very similar to those of the concentric case. However, at low frequencies unexpected artefacts arise in the damping graph. This low frequent behavivour is most probably due to the fact that the used timesteps are
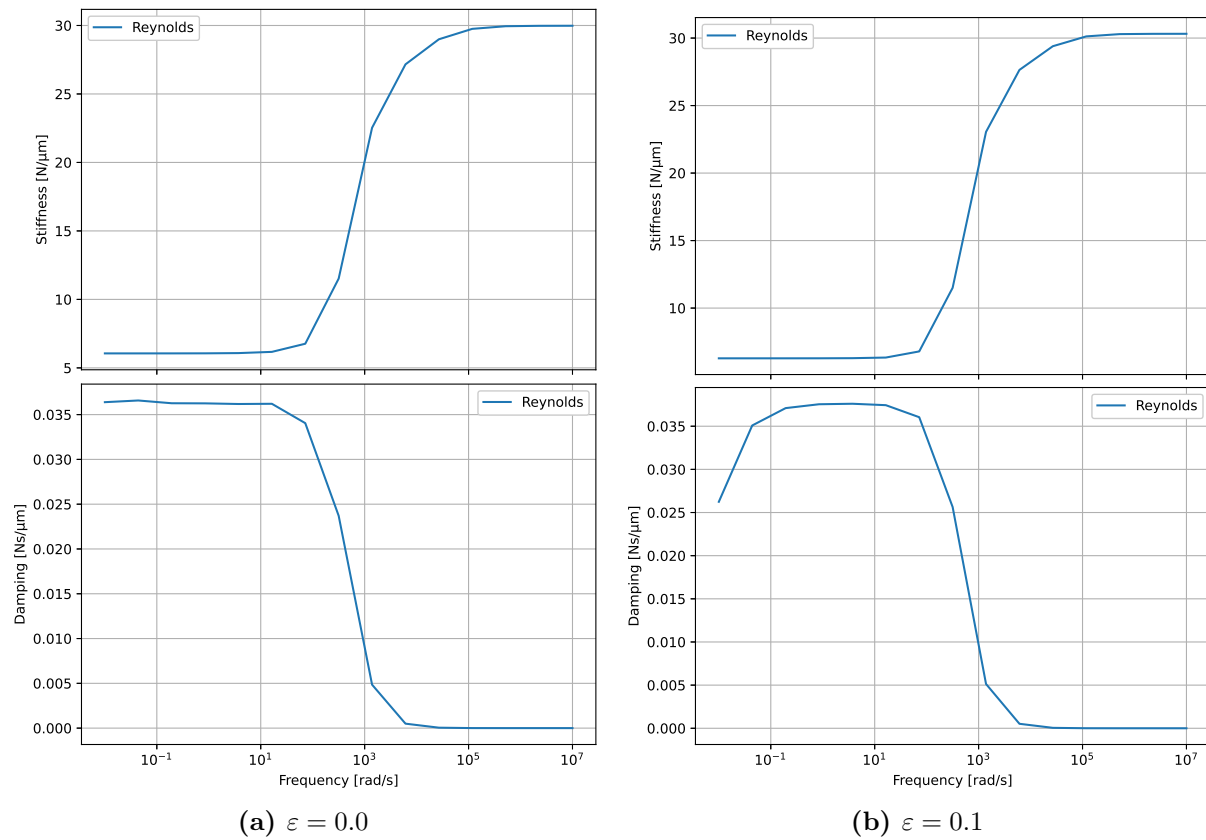
Figure 3.10. *Dynamic damping and stiffness as a function of pertubation frequency ω for $\varepsilon = 0.0$ and $\varepsilon = 0.1$.*

optimised for the applied input signal. This however neglects the presence of other time scales in the model which can cause this behaviour at low frequencies. Additionally, a small phase difference due to damping from the time integration potentially yields great errors in the low frequeny range. This because the dynamic damping is inversely proportionate with ω. This effect is also confirmed by the observation that for smaller time intervals the graph straightens.

Chapter 4

Reduced order modeling

To increase computational efficiency, a reduced order model (ROM) is created of the proposed model. Model order reduction aims to lower the computational complexity of mathematical and dynamical models by reducing its associated state space dimension. One rather obvious way to achieve this dimensionality reduction for a finite element model is to lower the number of degrees of freedom (dofs), i.e. coarsening the mesh. In Chapter 3, however, the dependecy of the model results to the mesh size and the disadvantages of grid coarsening is thoroughly discussed. Hence a different dimensionality-reduction technique is required.

Various methods are available to create a ROM of which many are based on the projection of known, high-dimensional dynamics onto a set of modes. These modes are obtained by a hierarchical modal decomposition that can be truncated at some reduced model order r. Consider a high-dimensional system written as a linear time invariant (LTI) system in descriptor form:

$$\mathbf{E}\dot{\mathbf{X}} = \mathbf{A}\mathbf{X} + \mathbf{B}\mathbf{U},$$
$$\mathbf{Y} = \mathbf{C}\mathbf{X} \tag{4.1}$$

The primary goal of model order reduction is to find a dedicated coordinate transformation $\mathbf{X} = \mathbf{T}\tilde{\mathbf{X}}$, to construct a related system in reduced dimensional space with similar input/output behaviour:

$$\tilde{\mathbf{E}}\dot{\tilde{\mathbf{X}}} = \tilde{\mathbf{A}}\tilde{\mathbf{X}} + \tilde{\mathbf{B}}\mathbf{U},$$
$$\mathbf{Y} = \tilde{\mathbf{C}}\tilde{\mathbf{X}} \tag{4.2}$$

To retrieve such a coordinate transformation and the resulting reduced order system, different methods can be used of which two will be accessed throughout this thesis. First, a system theory approach is applied which utilizes a linearization of the Reynolds equation around an equilibrium state. This allows one to apply balancing techniques to retrieve the best obeservable and controllable modes of the system. Secondly, a data-driven approach is applied that uses spatial-temporal data from, in this case, a simulation. This data can be used to construct a linear model of a possible strongly non-linear system and reducing it accoringly.

Both approaches have a different philosophy, advantages and disadvantages. In this chapter the development of a ROM of the proposed air bearing model is discussed using both approaches discussed above. The results of each approach will be discussed independently after which a comparison is made.

4.1 System theory approach

As stated before, the overarching reason for creating a ROM is to allow for real time applications of high dimensional models. In the case of an air bearing system this most likely means the deployment of a ROM within a feedback control loop, or as part of a larger FEM simulation. As these applications benefit more from the response of the input/output behaviour of this component, it is wise to explore system theory based approaches for creating a ROM. This implies the creation of an LTI representation of the Reynolds equation by means of linearization around an equilibrium state. In this way the state of the system is written in terms of shaft positions and velocities.

4.1.1 Linearization

Introducing the perturbed variables of the Reynolds equation as:

$$
\begin{aligned}
h &= h_0 + \delta h(t), \\
p &= p_0 + \delta p(t)
\end{aligned}
\tag{4.3}
$$

where p_0 and h_0 define the equilibrium state, and p and h are defined according to the finite element discretization with basis functions φ and ξ as:

$$
\begin{aligned}
p &= \varphi_i X_i, \\
h &= \xi_k^d U_k, \\
\dot{h} &= \xi_k^v \dot{U}_k
\end{aligned}
\tag{4.4}
$$

with the pressure dofs stored in X, position input in U and velocity input in $\dot{U}$. The linearization is then obtained by taking the Gateaux derivative of the bilinear and linear forms of the discretised Reynolds equation, as derived in Equation (3.2), allong the direction of φ and ξ. The equilibrium position around which the linearization is performed is defined as $\varepsilon = 0.0$ and $\dot{h} = 0$. The linearization is given according to Equations (4.5) to (4.7).

$$
\frac{\partial}{\partial_t}\mathcal{M}(p,\varphi) \cong \underbrace{\langle \partial_p \mathcal{M}_i, \varphi_j \rangle}_{E_{ij}} \dot{X}_j + \underbrace{\langle \partial_h \mathcal{M}_i, \xi_k^v \rangle}_{B_{ik}^v} \dot{U}_k
\tag{4.5}
$$

$$
\mathcal{B}(p,\varphi) \cong \underbrace{\langle \partial_p \mathcal{B}_i, \varphi_j \rangle}_{A_{ij}} X_j + \underbrace{\langle \partial_h \mathcal{B}_i, \xi_k^d \rangle}_{B_{ik}^d} U_k
\tag{4.6}
$$

$$
\mathcal{F}(\varphi) \cong \underbrace{\langle \partial_p \mathcal{F}_i, \varphi_j \rangle}_{C_{ij}} X_j
\tag{4.7}
$$

It turns out that the linearization of the squeeze term yields an additional input matrix B^v. This is however not treated as an additional input to the system, since the input $\dot{U}$ is directly computed as the time derivative of U, yielding a single-input single-output (SISO) system. Using the system matrices as described above, the LTI system can be written as:

$$
\begin{aligned}
\mathbf{E}\dot{\mathbf{X}} &= \mathbf{A}\mathbf{X} + \mathbf{B}^{\mathbf{d}}U + \mathbf{B}^{\mathbf{v}}\dot{U}, \\
Y &= \mathbf{C}\mathbf{X}
\end{aligned}
\tag{4.8}
$$

Taking the Laplace transform of Equation 4.8 and rearranging its terms, an expression for the transfer function (TF) of the Reynolds equation is yielded according to Equation (4.9). Where s is a complex frequency written as $s = i\omega$.

$$\mathbf{H}(s) = \frac{\mathbf{Y}(s)}{\mathbf{U}(s)} = \mathbf{C}(\mathbf{E}s - \mathbf{A})(\mathbf{B^d} + s\mathbf{B^v}) \tag{4.9}$$

To determine the performance of the linearization, both the static and dynamic coefficients are computed in the same manner as for the full non-linear FEM. The steady state problem is solved by excluding the time dependent terms in Equation (4.8), after which the system $\mathbf{AX} = -\mathbf{B^d}U$ can be solved. Figure 4.1 reports the static behaviour of the linearised system by simulating a small pertubation in ε, resulting in the perturbed pressure field given by Figure 4.1b. This result is then compared to a full FEM solution using the same pertubation as given by Figure 4.1a. The resulting error is computed as $|p^{fem} - p^{lti}|$ and normalised to the supply pressure p_s. It can be seen in Figure 4.1c that very favorable error values are achieved which are significantly lower than the accepted discretization errors discussed in Chapter 3. In terms of load capacity error, a relative error of 7.07×10^{-5} is found which is approximately the same order of magnitude as the error in the pressure solution.

For the dynamic coefficients, the frequency dependent results of the LTI system are compared to those of the full FEM solution. Figure 4.2 reports the frequency dependent dynamic coefficients of both the FEM and the LTI, using both $\varepsilon = 0.0$ and $\varepsilon = 0.5$. Figure 4.2a additionally contains the frequency response of the LTI system using a Crank-Nicolsen (CN) time discretization scheme to validate the time convergence of the LTI. From this analysis, the LTI system shows good convergence in time as it overlaps almost perfectly with the TF approach. This assures the exclusion of initial transients in the computation of the dynamic coefficients.

From both Figure 4.2a and Figure 4.2b it can be seen that the response of the LTI in the

(a) *Perturbed FEM.*

(b) *Perturbed LTI.*
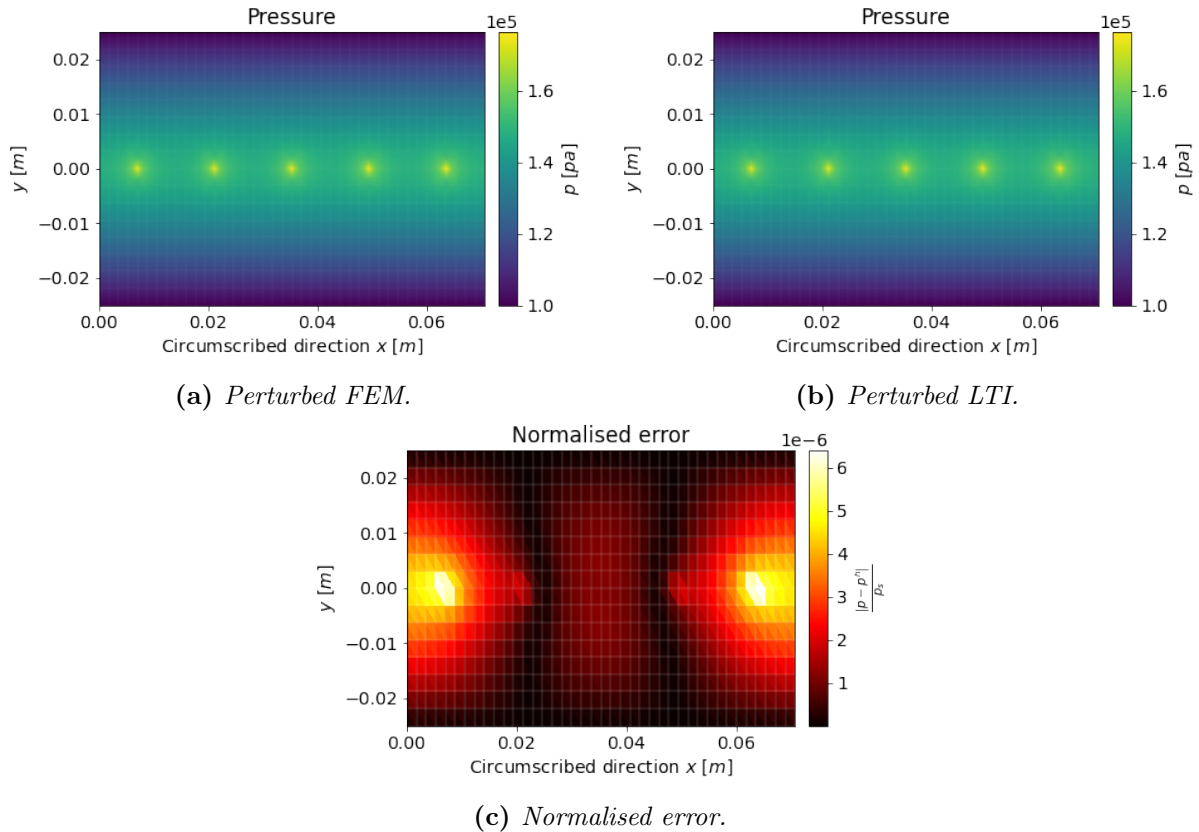

(c) *Normalised error.*

Figure 4.1. *Comparison of the static linearised Reynolds model with the full non-linear Reynolds model. For both simulations the same shaft perubation is applied of 10^{-7} m.*

low frequency range approaches the FEM solution. Both damping and stiffness coeffients have the same assymptotic behaviour at $\omega \to 0$ and $\omega \to \infty$. The squeeze film dynamics around $\omega = 10^2 \ Hz$ is also captured in both the stiffness and damping response. In contrary to the FEM solution for $\varepsilon = 0.1$, the LTI results for the damping at $\omega \to 0$ behave as one would expect without the artefacts visible in the FEM solution. Because the TF approach is only frequency dependent this strenghtens the observation made in Section 3.3.

The qualitiy of the linearization is examined through the error between the FEM and LTI solutions normalized to the FEM solution. Figure 4.3 reports the relative error as a function of pertubation frequency for both the stiffness and damping results at $\varepsilon = 0.0$. The error clearly increases around $100 \ Hz$ where the non-linear squeeze behaviour is dominant, yielding errror values much greater than the accepted discretization error. Considering both the static and dynamic behaviour, the LTI is able to capture the response of both the stiffness and damping characteristics. However, in terms of relative error one should be carefull in the range where the non-linear squeeze behaviour is dominant.

4.1.2 Balanced truncation

The linear system is allready significantly faster to solve than the full non-linear FEM, however, it still consists of the complete set of pressure dofs. Allthough the used model only consists of only a couple of hundred dofs, this number can grow rapidly to a couple of thousands when unstructured meshes are used, or adaptive mesh refinement is applied. Therefore a ROM is
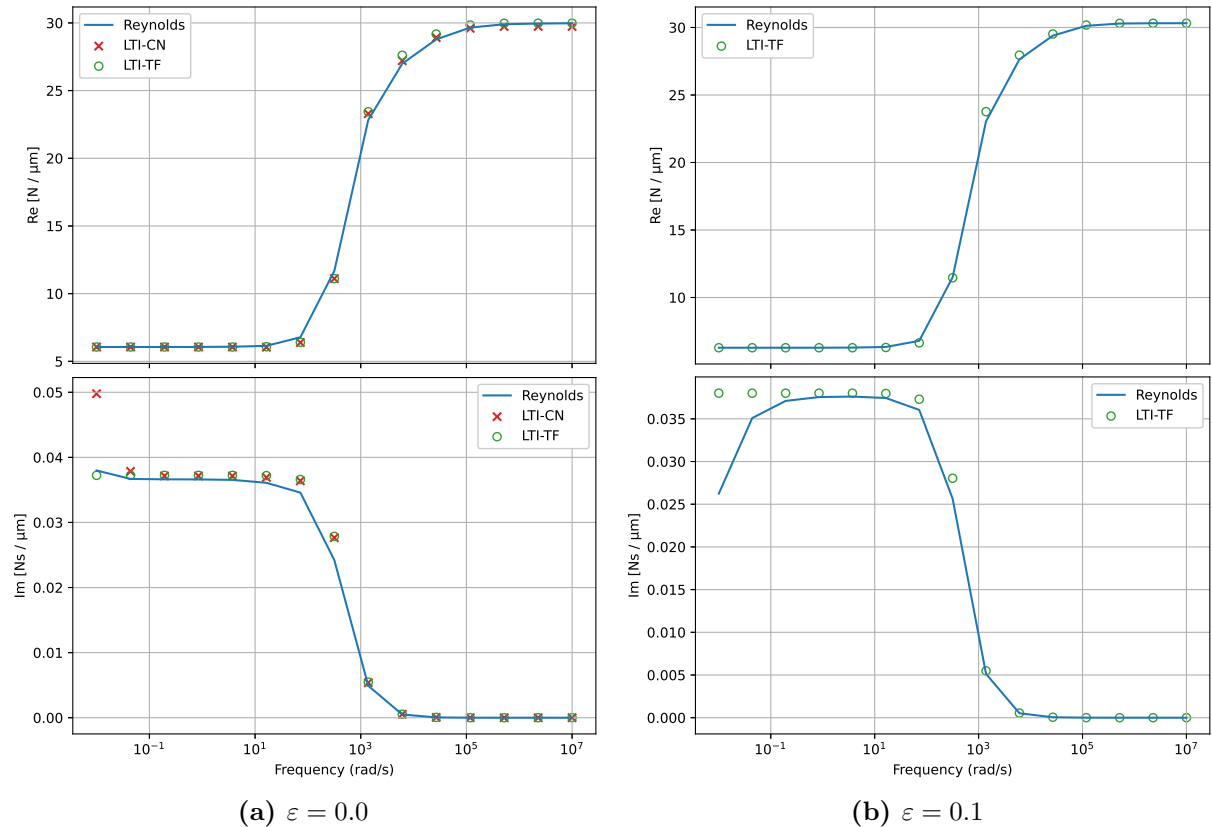

Figure 4.2. *LTI performance compared to the non-linear FEM solution in terms of the dynamic stiffness and damping as a function of pertubation frequency ω. In Figure 4.2a the transient LTI is solved using a Crank-Nicolsen scheme which shows proper convergence in time.*
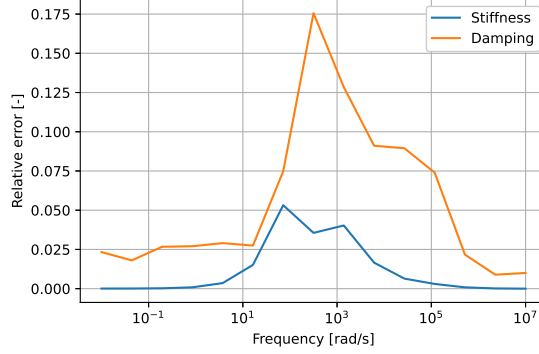
Figure 4.3. *Relative error of the dynamic stiffness and damping for $\varepsilon = 0.0$.*

constructed by using the balanced truncation method (BT), first introduced by B.C. Moore [26]. This method is based on the introduction of a balanced realization of the full-order LTI system and truncating it accordingly. This implies the discovery of a coordinate transformation that captures the most controllable and observable states in the system. In this way the stability of the system is preserved, which is a major advantage of BT. An additional advantage is the definition of a-priori computable upper and lower error bounds for the system error [27]. Starting from the full-order realization of the LTI given by Equation (4.8), the balancing problem can be defined as:

$$
\begin{cases}
\text{Find the invertible coordinate transformation matrices } T, S \in \mathbb{R}^{n \times n}, \\
\text{such that the realization with:} \\
\hat{E} = S^T E T = I \\
\hat{A} = S^T A T \\
\hat{B} = S^T B \\
\hat{C} = C T \\
\text{has Gramians } \mathcal{P} \text{ and } \mathcal{Q} \text{ satisfying :} \\
\mathcal{P} = \mathcal{Q} = \Sigma^H = \text{diag}(\sigma_i^H)
\end{cases} \tag{4.10}
$$

with the Hankel singular values σ_i^H. The controlability ($\mathcal{P}$) and observability ($\mathcal{Q}$) gramians are defined as:

$$
\mathcal{P} = \int_0^\infty e^{A\tau} B B^* e^{A^*\tau} d\tau \tag{4.11}
$$

$$
\mathcal{Q} = \int_0^\infty e^{A^*\tau} C^* C e^{A\tau} d\tau \tag{4.12}
$$

In geneneral it is rather impractical to compute the controllability and observability Gramians directly from Equation (4.11) and Equation (4.12). Instead these Gramians are computed by solving the Lyapunov equations given by Equation (4.13)

$$
0 = \mathbf{A}\mathcal{P} + \mathcal{P}\mathbf{A}^* + \mathbf{B}\mathbf{B}^*
$$
$$
0 = \mathbf{A}^*\mathcal{Q} + \mathcal{Q}\mathbf{A} + \mathbf{C}^*\mathbf{C} \tag{4.13}
$$

Remark 4.1.1. *It should be taken into account that solving the Lyapunov equations for high-dimensional systems is numerically rather expensive [28]. For these systems it would be beneficial*

to approximate the gramians using experimental or numerical data instead as showed in [29].

The truncation of the model is based on the controllability and observability energies of the states. These energy functions define the minimum energy to steer the system from the zero state to the next, and the energy of the output at that next state. Given that $\mathcal{P}$ is invertible, the controllability and observabillity energies are given by respectively Equation (4.14) and Equation (4.15):

$$\mathcal{E}_c = \mathbf{x}^* \mathcal{P}^{-1} \mathbf{x} \tag{4.14}$$

$$\mathcal{E}_o = \mathbf{x}^* \mathcal{O} \mathbf{x} \tag{4.15}$$

Relating the energy functions to the fact that $\mathcal{P}$ and $\mathcal{Q}$ are equal to Σ, it becomes clear that the states corresponding to the smallest Hankel singular values are the most difficult to reach and observe. A truncated model can therefore be defined by defining two basis matrices $V, W \in \mathbb{R}^{n \times r}$ as the first r columns of T and S, yielding a ROM as:

$$\begin{aligned} \tilde{\mathbf{E}}\dot{\tilde{\mathbf{X}}}(t) &= \tilde{\mathbf{A}}\tilde{\mathbf{X}}(t) + \tilde{\mathbf{B}}U(t) \\ Y(t) &= \tilde{\mathbf{C}}\tilde{\mathbf{X}}(t) \end{aligned} \tag{4.16}$$

where $\tilde{\mathbf{E}} = W^{\mathrm{T}}\mathbf{E}V$, $\tilde{\mathbf{A}} = W^{\mathrm{T}}\mathbf{A}V$, $\tilde{\mathbf{B}} = W^{\mathrm{T}}\mathbf{B}$, $\tilde{\mathbf{C}} = \mathbf{C}V$ [27, 29, 30].

Error bounds

As stated above, computable a-priori error bounds are defined for the BT method. The $\mathcal{H}_\infty$ norm of the error between the transfer functions of the full-order model and the ROM is bounded according to the upper and lower bounds described by Equation (4.17) and Equation (4.18) respectively [27].

$$\|H(s) - \tilde{H}(s)\|_{\mathcal{H}_\infty} \le 2 \sum_{i=r+1}^{n} \sigma_i \tag{4.17}$$

$$\|H(s) - \tilde{H}(s)\|_{\mathcal{H}_\infty} \ge \sigma_{r+1} \tag{4.18}$$

Figure 4.4 reports the upper and lower a-priori error bounds for the LTI system for all possible model orders r. A rapid decay of the error is observed at the first couple of model orders for
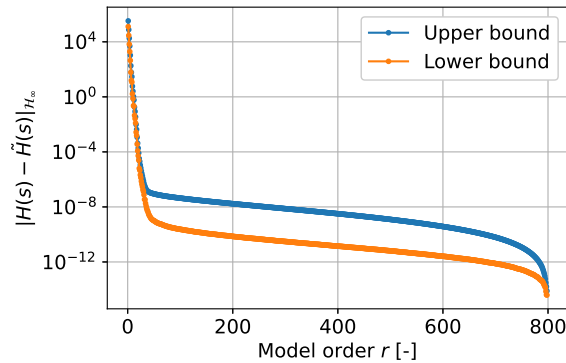

Figure 4.4. *Upper and lower a-priori error bounds of the balanced LTI model for $\varepsilon = 0.0$.*

both the upper and lower bound. A ROM that utilizes the first 20 balanced states yields an upper bound error of approximately 10^{-8}. This is significantly lower than the linearization error defined above.

Figure 4.5 reports the frequency response of the balanced LTI truncated at various model orders. Figure 4.5a contains the results for $\varepsilon = 0.0$, which shows relative fast convergence towards the full-order LTI model. The results for $\varepsilon = 0.4$ in Figure 4.5b shows a slower convergence. The ROMs of which its respective model order is too low are underestimating the stiffness at high frequencies, while overestimating the damping at lower frequencies. The ROM of order $r = 20$ shows to be a good approximation of the full order LTI for both zero and non-zero eccentricity. To confirm this observation, the frequency dependent magnitudes of the error between the full-order model and a ROM of order 20 for both $\varepsilon = 0.0$ and $\varepsilon = 0.4$ are reported in Figure 4.6. From this figure the a-priori $\mathcal{H}_\infty$ norm of the error is visible as the maximum value of the error magnitude of the $\varepsilon = 0.0$ case. Alltough the eccentric case has an error magnitude of 3 orders of magnitude higher than the concentric case, it is still significantly lower than the linearization

Table 4.1. *Comparison of the simulation times betweem the full non-linear FEM, the full-order LTI system and a ROM of order 20.*

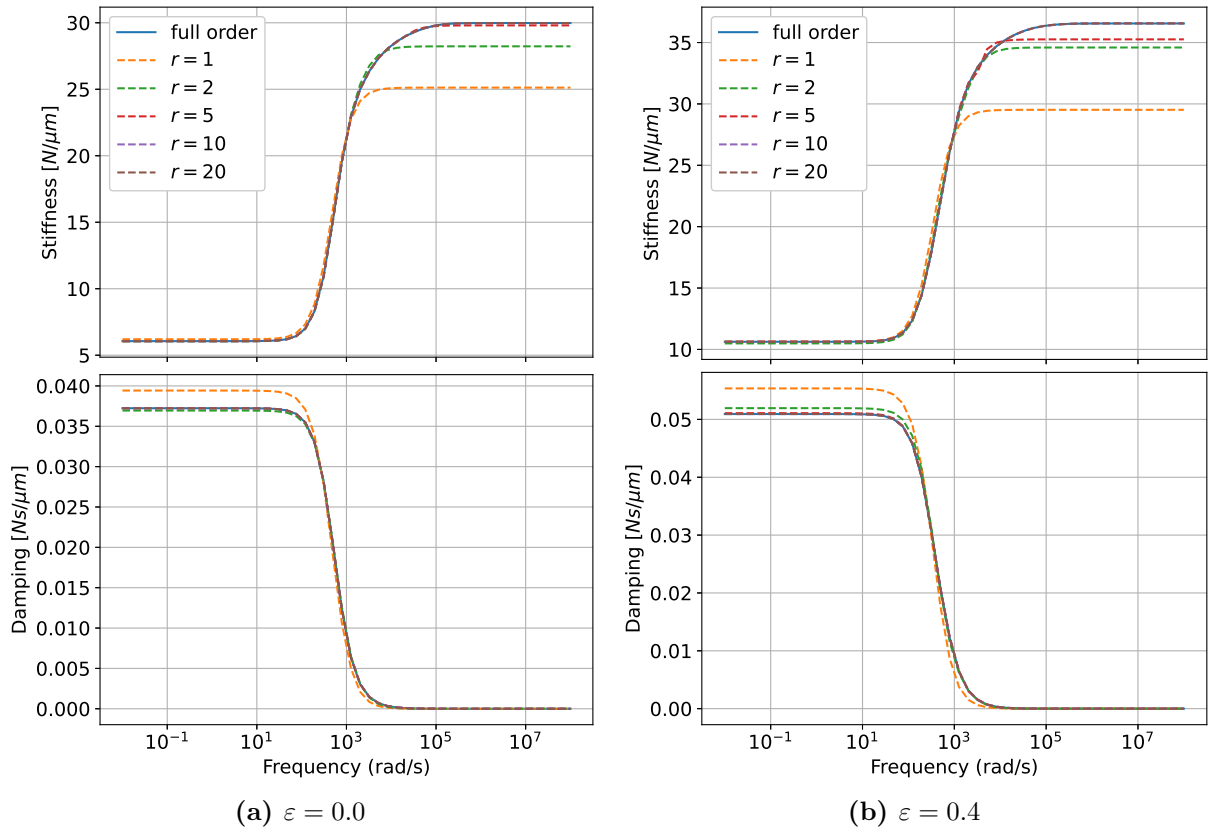| Model order r	Simulation time [s]
FEM	6673.34
LTI	23.87
ROM r=20	2.54

(a) $\varepsilon = 0.0$

(b) $\varepsilon = 0.4$

Figure 4.5. *Dynamic results of the balanced LTI truncated at increasing model order r, for both $\varepsilon = 0.0$ and $\varepsilon = 0.4$.*
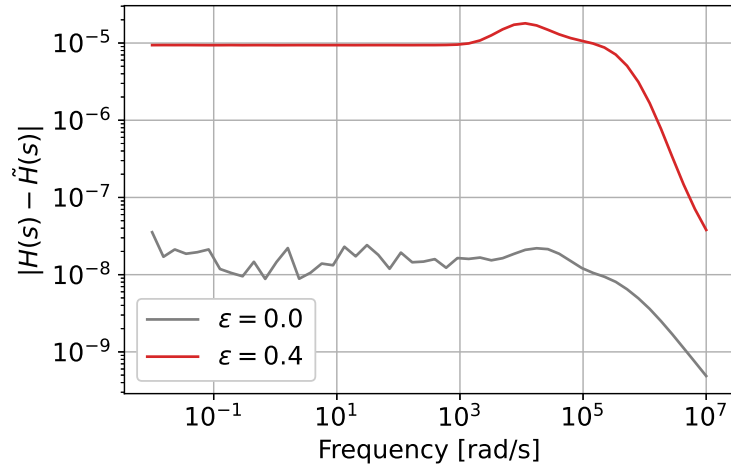
Figure 4.6. *Magnitude of the error between the full-order model and a ROM of order 20 for $\varepsilon = 0.0$ and $\varepsilon = 0.4$.*

error. Both graphs show a further decrease in error in the higher frequency range.

The improved efficiency of the ROM is accessed through the comparison of the computational time used to solve a transient problem. To that end, the transient response to a step input of both the full-order LTI and the ROM of order 20 are computed and reported in Figure 4.7. From this figure it is clear that the ROM again shows good performance compared to the full-order LTI system, now for inputs using multiple frequencies. For both systems the transient response is solved using a CN scheme and a timestep of 10^{-5}. The computational time of both simulations, and of a non-linear FEM simulation using the same number of timesteps, are listed in Table 4.1. The table shows a reduction in computational time of the ROM compared to the LTI with a factor of around 10.

Figure 4.7. *Transient response to a step input of 10^{-6} for the full-order LTI model and a ROM of order 20. The transient simulation is solved using a CN scheme and a timestep of 10^{-5} for $\varepsilon = 0.0$.*

4.2 Data-driven approach

Data-driven approaches are widely used for model order reduction. Methods such as the proper orthogonal decomposition (POD) and the dynamic mode decomposition (DMD) have proved their contribution to the model reduction of large s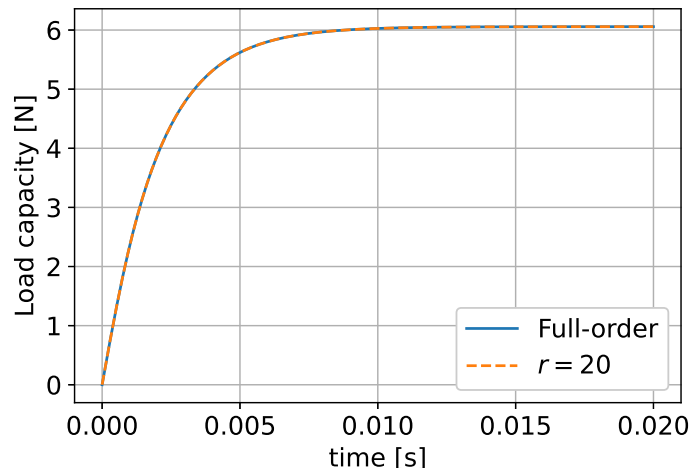cale fluid dynamical problems [29, 31]. DMD is based on POD and both methods utilizes the singular value decomposition (SVD), which make these methods computaionally efficient and attractive. POD provides a modal decomposition solely based on the SVD that hierarchically orders its modes in terms of spatial correlation and energy content. In contrast to POD, DMD provides a modal decomposition of which each mode consists of spatially correlated structures that have the same linear behaviour in time. An advantage of these data-driven methods over the model-based methods, as discussed in the previous section, is that no prior knowledge of the system is required. These methods are completely equation free and may be applied utilizing just collected data from the system.

4.2.1 Dynamic mode decomposition

DMD was first introduced by Schmid et al. [31, 32] to identify spatio-temporal coherent structures from high-dimensional data. The original DMD method utilizes a Krylov subspace method, a variant of the commonly used Arnoldi iteration, where it searches for the best-fit linear operator $\mathbf{A}$ that advances high-dimensional measurements of a potentially non-linear system in time as:

$$\mathbf{X}' \approx \mathbf{A}\mathbf{X} \tag{4.19}$$

Different algorithms exist to compute this operator, here only the standard SVD-based algorithm (SDMD), as presented in [32], is considered. Because DMD is inherently data-driven, it requires measurements or snapshots of the system. Therefore, solutions to the non-linear FEM problem are aranged in two matrices $\mathbf{X}$ and $\mathbf{X}'$, as the system evolves in time. These snapshot matrices are constructed according to Equation (4.20) and (4.21), with the total number of snapshot matrices s. For very high-dimensional systems the computation of $\mathbf{A}$ and its spectral decomposition becomes intractable. The SDMD therefore provides an algorithm that leverages dimensionality reduction to compute the spectral decomposition of $\mathbf{A}$, without the necessity of computing $\mathbf{A}$ directly. The SDMD algorighm is described in Algorithm 1.

$$\mathbf{X} = \begin{bmatrix} | & | & & | \\ \mathbf{x}_1 & \mathbf{x}_2 & \cdots & \mathbf{x}_{s-1} \\ | & | & & | \end{bmatrix} \tag{4.20}$$

$$\mathbf{X}' = \begin{bmatrix} | & | & & | \\ \mathbf{x}_2 & \mathbf{x}_3 & \cdots & \mathbf{x}_s \\ | & | & & | \end{bmatrix} \tag{4.21}$$

Control

The DMD as described above was initially developed to identify naturally evolving systems [29]. A prominent example of this in which the strengths of DMD emanate is for instance the flow around a cylinder [33]. This however does not account for the effect of any forcing or control of the system, which for the case of an air bearing component in a high performance application would be opportune. The DMD with control (DMDc) by Proctor et al. [34] is an extension to the DMD algorithm where the unforced dynamics is seperated from the effect of actuation. This method essentially differs from SDMD in the sense that an additional measurement is added to

the system. The aim of DMDc is to search for the best fit linear operators A and B that relates the snapshot matrices X' and X and the control input Υ best in time as:

$$\mathbf{X}' \approx \mathbf{A}\mathbf{X} + \mathbf{B}\Upsilon \tag{4.22}$$

DMDc is described by Algorithm 2. It utilizes the beneficial properties of SDMD in the sense that both $\mathbf{A}$ and $\mathbf{B}$ are not computed directly. The method requires the definition of an additional third snapshot matrix Υ, which contains the actuation input of the system as given by Equation (4.23). The resulting reduced order operators $\tilde{\mathbf{A}}$ and $\tilde{\mathbf{B}}$ may be used to construct a reduced order state space realization by the assignment of $\tilde{\mathbf{C}}$. This method is not used within this thesis, however, it is a promising approach. In Appendix B it is therefore briefly elaborated further.

$$\Upsilon = \begin{bmatrix} | & | & & | \\ \mathbf{u}_1 & \mathbf{u}_2 & \cdots & \mathbf{u}_{s-1} \\ | & | & & | \end{bmatrix} \tag{4.23}$$

4.2.2 Stability of the ROM

To showcase the SDMD and the DMDc algorithms on the proposed air bearing model, a trivial case is examined through the process of data reconstruction. Therefore the matrices $\mathbf{X}$ and $\mathbf{X}'$ are constructed using the frequency response data from a transient FEM simulation as described in Section 3.3. The pertubation signal applied to the shaft is used as a control input stored in Υ.
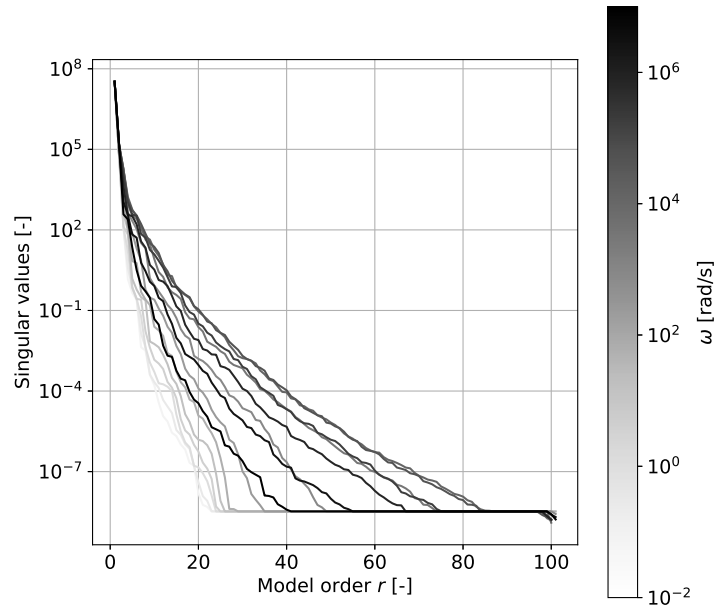

Figure 4.8. *Singular values of the snapshot matrices constructed at increasing values of ω.*

Algorithm 1 SDMD

Find dynamic properties of:
$\mathbf{X}' \approx \mathbf{A}\mathbf{X}$

1. Compute truncated SVD of $\mathbf{X}$:
   $\mathbf{X} \approx \tilde{\mathbf{U}}\tilde{\boldsymbol{\Sigma}}\tilde{\mathbf{V}}^*$

2. Compute pseudo-inverse of $\mathbf{X}$:
   $\mathbf{X}^\dagger = \mathbf{V}\boldsymbol{\Sigma}^{-1}\mathbf{U}^*$

3. Compute reduced-order approximation of $\mathbf{A}$:
   $\tilde{\mathbf{A}} = \mathbf{X}'\mathbf{X}^\dagger = \mathbf{X}'\tilde{\mathbf{V}}\tilde{\boldsymbol{\Sigma}}^{-1}\tilde{\mathbf{U}}^*$

4. Spectral decomposition of $\tilde{\mathbf{A}}$:
   $\tilde{\mathbf{A}}\mathbf{W} = \mathbf{W}\boldsymbol{\Lambda}$

5. Compute dynamic modes:
   $\boldsymbol{\Phi} = \mathbf{X}'\tilde{\mathbf{V}}\tilde{\boldsymbol{\Sigma}}^{-1}\mathbf{W}$

6. Spectral expansion:
   $\mathbf{X}(k\Delta t) = \boldsymbol{\Phi}\boldsymbol{\Lambda}^t b$

Algorithm 2 DMDc

Find dynamic properties of:
$\mathbf{X}' \approx \mathbf{A}\mathbf{X} + \mathbf{B}\boldsymbol{\Upsilon}$

1. Construct input matrix:
   $\boldsymbol{\Omega} = [\mathbf{X}, \boldsymbol{\Upsilon}]^\top$

2. Compute truncated SVD of input matrix:
   $\boldsymbol{\Omega} \approx \tilde{\mathbf{U}}\tilde{\boldsymbol{\Sigma}}\tilde{\mathbf{V}}^* = [\mathbf{X}, \boldsymbol{\Upsilon}]\tilde{\boldsymbol{\Sigma}}\tilde{\mathbf{V}}^*$

3. Compute truncated SVD of output matrix:
   $\mathbf{X}' \approx \hat{\mathbf{U}}\hat{\boldsymbol{\Sigma}}\hat{\mathbf{V}}^*$

4. Reduced-order approximation of A:
   $\tilde{\mathbf{A}} = \hat{\mathbf{U}}^*\mathbf{X}'\tilde{\mathbf{V}}\tilde{\boldsymbol{\Sigma}}^{-1}\tilde{\mathbf{U}}_1^*\hat{\mathbf{U}}$

5. Reduced-order approximation of B:
   $\tilde{\mathbf{B}} = \hat{\mathbf{U}}^*\mathbf{X}'\tilde{\mathbf{V}}\tilde{\boldsymbol{\Sigma}}^{-1}\tilde{\mathbf{U}}_2^*$

6. Eigen decomposition:
   $\tilde{\mathbf{A}}\mathbf{W} = \mathbf{W}\boldsymbol{\Lambda}$

7. Compute dynamic modes:
   $\boldsymbol{\Phi} = \mathbf{X}'\mathbf{V}\tilde{\boldsymbol{\Sigma}}^{-1}\tilde{\mathbf{U}}_1^*\hat{\mathbf{U}}\mathbf{W}$

Remark 4.2.1. *Algorithm 2 describes the DMDc algorithm for the case B is fully unknown. However, it is worth mentioning that in [34] an additional algorithm is developed for the case that* $\mathbf{B}$ *is known.*

To determine a suffieciently large model order, the energy content of each SVD mode of the snapshot matrix is examined in terms of the corresponding singular values. Figure 4.8 reports the singular values of the snapshot matrices constructed with training data at different values of ω. From this figure it can be concluded that for all cases almost all of the energy of the system is contained within the first 20 to 40 SVD modes. From the figure the increasing dominance of the squeeze dynamics can be observed, since for the mid frequency range more modes are required to contain the same energy content.

In contrast to BT, the initial stability of a system in not preserved. Hence the stability of the retrieved reduced order SDMD and DMDc dynamical systems should be carefully examined. The stability is analysed in Figure 4.10, showing the size of the eigenvalues of both the SDMD and DMDc $\tilde{\mathbf{A}}$ operators, with respect to the unit circle. Figures $4.10a - 4.10c$ contain the stability results of the SDMD, and Figures $4.10d - 4.10f$ contain the stability results of the DMDc. Both operators are trained at three different frequencies and truncated at $r = 25$. It can be seen that for all cases the eigenvalues lie within the unit circle, resulting in stable systems. Only at $\omega = 10^7$ a non stable eigenvalue appears. However, the time scale of the pertubation at this frequency is suffieciently short that no unstable behaviour is expected in the first couple of periods in the transient response.

The stability results of the reduced order systems trained at $\varepsilon > 0.0$ are very similar to those reported for the systems trained at $\varepsilon = 0.0$. For $\omega = 10^{-2}$, however, the DMDc operator has slightly unstable eigenvalues as can be seen in Figure 4.9. Because the time scales of the pertubation are relatively large, this slight instability will cause the transient response to diverge.

4.2.3   Reconstruction of transient response

With the computed operators, the transient response is reconstructed using the first column of both $\mathbf{X}$ and $\mathbf{\Upsilon}$ as an initial condition. Figure 4.11 reports the reconstructed response of both the SDMD and DMD for the three different frequencies. As expected, DMD is able to reconstruct its response very well. However, DMDc is showing some unexpected behaviour at lower frequencies.

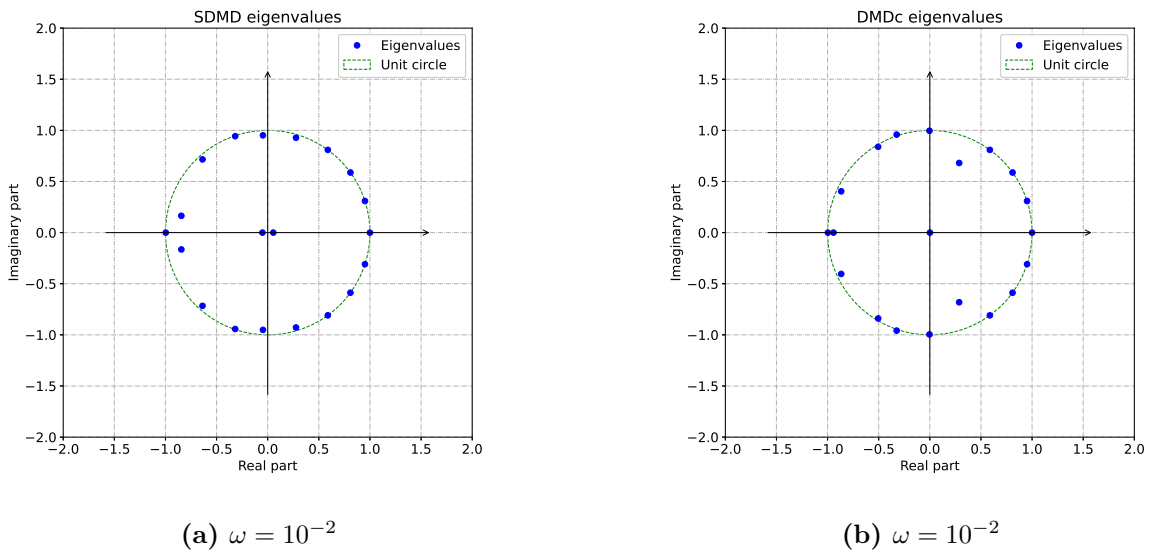**(a)** $\omega = 10^{-2}$ **(b)** $\omega = 10^{-2}$

Figure 4.9. *Eigenvalues of both the EDMD and DMDc $\tilde{\mathbf{A}}$ operators of order 25 with respect to the unit circle. The operators are trained at $\omega = 10^{-2}$ and $\varepsilon = 0.4$.*

(a) $\omega = 10^{-2}$

(b) $\omega = 10^{-2}$

(c) $\omega = 10^2$

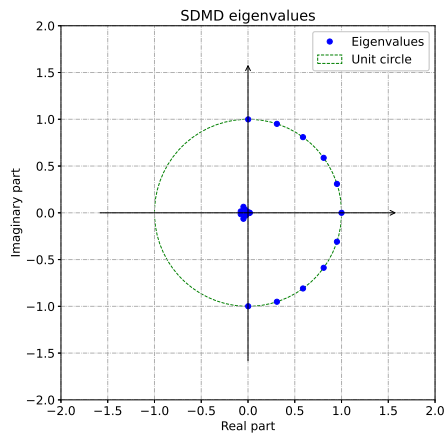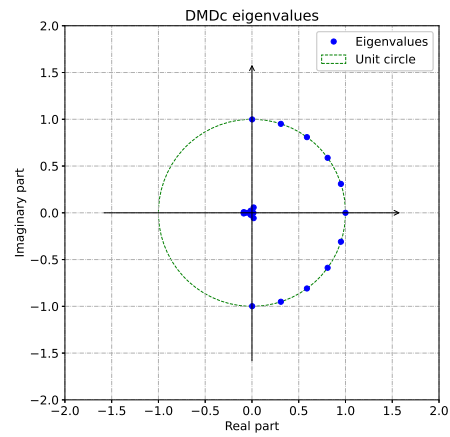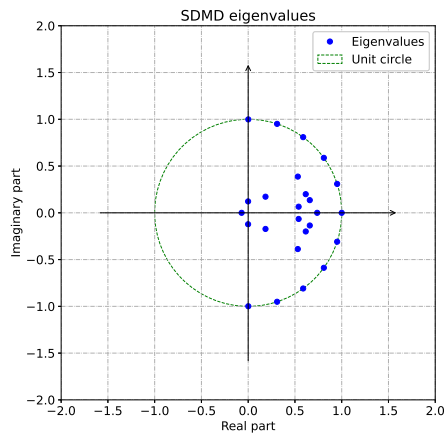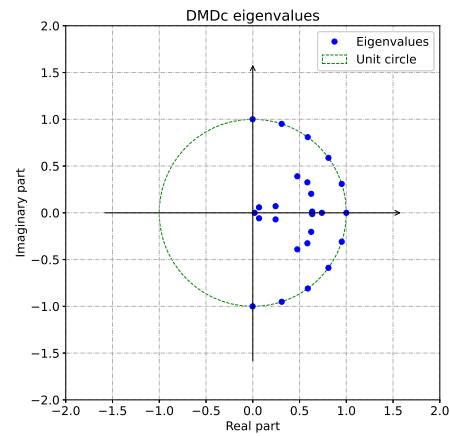**(d)** $\omega = 10^2$
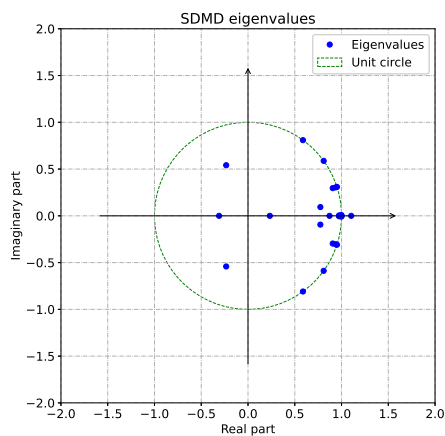
(e) $\omega = 10^7$
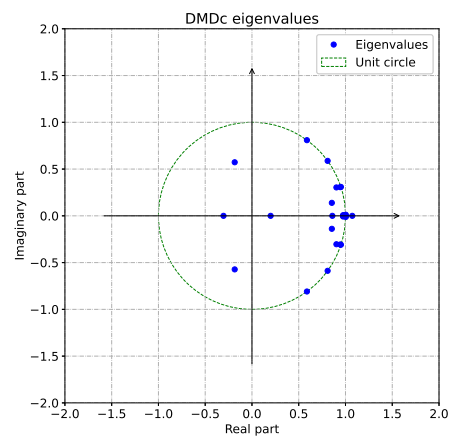
(f) $\omega = 10^7$

Figure 4.10. *Eigenvalues of both the SDMD and DMDc* $\tilde{\mathbf{A}}$ *operators of order 25 with respect to the unit circle. The SDMD results are depicted in* $4.10a - 4.10c$ *, the DMDc results are depicted in* $4.10d - 4.10f$. *The operators are trained for three different frequencies, all at* $\varepsilon = 0.0$.

The reason of this is however not completely clear. A possible reason could be that the amplitude of the input signal is too low for the time scales present at lower frequencies. In that case the DMDc algorithm is effectively trying to approximate noise and is not able to seperate the unforced dynamics and the input. This is also observed in the fact that the reduced DMDc model is insensitive to any perturbation of the input. Further research, utilizing more suitable data generation methods, is required to obtain a sound understanding of these results.

(a) $\omega = 10^{-2}$ **(b)** $\omega = 10^{2}$ **(c)** $\omega = 10^{7}$

Figure 4.11. *Reconstructed transient responses using the reduced order SDMD and DMDc operators, trained at different values of ω. All in comparison with the full non-linear response.*

Chapter 5

Conclusion and discussion

The use of high fidelity models in analysing functional modules of complex mechatronic systems allows the utilization of more accurate predictions. However, these models often come at great computational 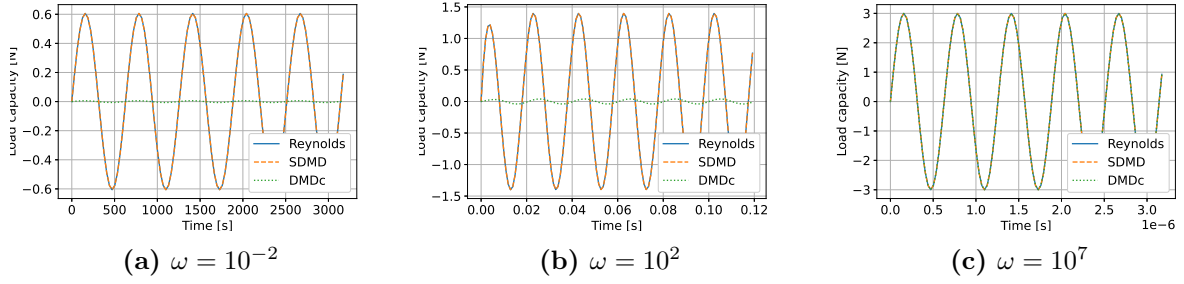costs. In this master thesis the development and reduction of a finite element model of an inherently compensated journal gas bearing is elaborated.

The proposed high fidelity finite elment model is based on the Reynolds equation. The model is able to describe the static and dynamic characteristics of the bearing for various geometries and input parameters. A thorough convergence study showed good convergence of the pressure solution and the computed characteristics, on structured uniform grids. Both of which are in correspondance to results found in literature. However, for larger orifice diameters, the proposed point source approach to model the orifices proved to be disadvantageous for the convergence of both the mass flow residual and load capacity. Due to the presence of steep pressure gradients, the solutions converge significantly slower resulting in impractical mesh sizes. Two altered approaches are therefore suggested. Firstly, utilizing adaptive mesh refinement and secondly, the consideration of the orifices as small but finite areas.

A linearization of the finite element model is constructed to allow for a more system theoretic approach. Significant linearization errors arise around the frequencies at which the non-linear squeeze dynamics become dominant. A good understanding of the operating domain of the bearing should determine whether this linearization error is acceptable or not. This ofcourse is strongly related to the application of the bearing and the loads it has to carry. The proposed balanced linearization truncated at order 20 is able to approach the linearization with a maximum error of approximately 10^{-5}. An efficiency increase of a factor 10 is achieved in terms of computational costs. Regardless of the favorable efficiency and implementation of BT, it should be taken into account that this ROM approach is not very well scalable to larger systems.

An alternative method is found in data-driven ROM approaches. Two variants of the dynamic mode decomposition are applied to the bearing case by reconstructing transient data. The original DMD algorithm is very well able to reproduce the transient response at a given frequency, only utilizing a few dynamic modes. However, this method is unable to include any form of actuation or control. Therefore, DMDc is introduced which seperates the naturally evolving system from the control input. Using the same transient data as for the DMD, the DMDc is not able to produce a similar reconstruction. Assumably the input pertubation is not defined well enough for a proper separation. Therefore it is recommended to explore more suitable data generation methods that better define the input signal.

5.1 Recommendations and future research

The proposed model is based on the Reynolds equation and therefore several assumptions have been made. Although these assumptions are discussed and acknowledged, their specific contribution to the solutions remain unknown. A comparison with experiments or a model based on the full navier-stokes equations may elucidate the effect of these assumptions.

To determine the dynamic behaviour of the bearing it is assumed that the shaft only deflects in the radial direction. However, in practice the shaft is also able to tilt relatively to the bush. This tilt behaviour is quantified through the tilt stiffness and is an important characteristic of the bearing performance. The ability of the proposed model and its reductions to predict this tilt stiffness is not included in this work. Further research should determine if adjustments to the model and the ROM approaches are required to capture the full dynamics if tilt is included.

In this work only the inherently compensated orifices are considered. However, the current implementation of the gas bearing model allows for other types of orifice restrictors, e.g. pocketed compensated or slot entry journal bearings. These types of orifices have different advantages over one another as elaborated in [16]. These orifice can be implemented through the definition of a suitable film height function $h(\theta)$, taking into account the limits of the thin film assumption.

The generation of trainig data for the DMD is conducted by isolating the transient response of the Reynolds equation at a given frequency. This results in relatively clean data with only a few frequencies that are present in the output of the model. It is shown that DMDc benefits from training data with clear defined actuation. A more advanced method of data generation to train the DMDc model is therefore advised. This may be achieved by the persistent excitation of the system, e.g., applying a gaussian noise signal to the system. In this way multiple frequencies are applied to the input while maintaining a workable time step size. The current implementation of the model does not allow for such random input signals. An alteration of the implementation of the transient solver is therefore required.

Bibliography

[1] Y. Maday and O. Mula. "A Generalized Empirical Interpolation Method: application of reduced basis techniques to data assimilation". In: *Springer INdAM Series* 4 (Dec. 2015), pp. 221–235. DOI: 10.1007/978-88-470-2592-9_13. arXiv: 1512.00683.

[2] Clarence W. Rowley et al. "Reduced-order models for flow control: Balanced models and Koopman modes". In: *IUTAM Bookseries*. Vol. 18. 2010, pp. 43–50. ISBN: 9789048137220. DOI: 10.1007/978-90-481-3723-7_6.

[3] Igor Mezić. "Spectral Properties of Dynamical Systems, Model Reduction and Decompositions". In: *Nonlinear Dynamics 2005 41:1* 41.1 (Aug. 2005), pp. 309–325. ISSN: 1573-269X. DOI: 10.1007/S11071-005-2824-X.

[4] Vladimir Kodnyanko et al. "Numerical Modeling on the Compliance and Load Capacity of a Two-Row Aerostatic Journal Bearing with Longitudinal Microgrooves in the Inter-Row Zone". In: *Applied Sciences 2021, Vol. 11, Page 5714* 11.12 (June 2021), p. 5714. ISSN: 2076-3417. DOI: 10.3390/APP11125714. URL: https://www.mdpi.com/2076-3417/11/12/5714/htm%20https://www.mdpi.com/2076-3417/11/12/5714.

[5] Farid Al-Bender. "On the modelling of the dynamic characteristics of aerostatic bearing films: From stability analysis to active compensation". In: *Precision Engineering* 33.2 (Apr. 2009), pp. 117–126. ISSN: 0141-6359. DOI: 10.1016/J.PRECISIONENG.2008.06.003.

[6] Claudio E. Merelli et al. "Dynamic Coefficients of Finite Length Journal Bearing. Evaluation Using a Regular Perturbation Method". In: *International Journal of Mechanical Sciences* 151 (Feb. 2019), pp. 251–262. ISSN: 00207403. DOI: 10.1016/J.IJMECSCI.2018.11.018. URL: https://doi.org/10.1016/j.ijmecsci.2018.11.018.

[7] Hakwoon Kim, Gunhee Jang, and Heonjeong Ha. "A generalized Reynolds equation and its perturbation equations for fluid dynamic bearings with curved surfaces". In: *Tribology International* 50 (June 2012), pp. 6–15. ISSN: 0301-679X. DOI: 10.1016/J.TRIBOINT.2011.12.019.

[8] Christopher Müller et al. "A Finite Element Analysis of Air Bearings Applied in Compact Air Bearing Spindles". In: *Procedia CIRP* 58 (Jan. 2017), pp. 607–612. ISSN: 2212-8271. DOI: 10.1016/J.PROCIR.2017.03.337.

[9] Gang Lin, Tojiro Aoyama, and Ichiro Inasaki. "A computer simulation method for dynamic and stability analyses of air bearings". In: *Wear* 126.3 (Sept. 1988), pp. 307–319. ISSN: 00431648. DOI: 10.1016/0043-1648(88)90172-X.

[10] W. T. Rouleau and L. I. Steiner. "Hydrodynamic Porous Journal Bearings. Part I—Finite Full Bearings". In: *Journal of Lubrication Technology* 96.3 (July 1974), pp. 346–353. ISSN: 0022-2305. DOI: 10.1115/1.3451962. URL: https://asmedigitalcollection.asme.org/tribology/article/96/3/346/418534/Hydrodynamic-Porous-Journal-Bearings-Part-I-Finite.

[11]   Krzysztof Czolczynski. "Rotordynamics of Gas-Lubricated Journal Bearing Systems". In: Mechanical Engineering Series (1999). DOI: 10.1007/978-1-4612-1518-9. URL: http://link.springer.com/10.1007/978-1-4612-1518-9.

[12]   W. B. (William Brian) Rowe. *Hydrostatic, aerostatic, and hybrid bearing design.* Elsevier, 2012, p. 333. ISBN: 9780123972392.

[13]   William A. Gross. *Gas film lubrication.* New York, Wiley, 1962, 413 pages.

[14]   Bernard J Hamrock, Steven R Schmid, and Bo O Jacobson. *Fundamentals of fluid film lubrication.* New York : Marcel Dekker, 2004, xiv, 699 pages : ISBN: 0824753712.

[15]   A. Z. Szeri. *Fluid film lubrication : theory and design.* Cambridge ; Cambridge University Press, 1998, xi, 414 pages : ISBN: 0521481007.

[16]   Alexander H. Slocum. *Precision machine design.* Dearborn, Mich. : Society of Manufacturing Engineers, 1992, xv, 750 pages : ISBN: 0872634922.

[17]   F. A. Al Bender and H. Van Brussel. "A Method of "Separation of Variables" for the Solution of Laminar Boundary-Layer Equations of Narrow-Channel Flows". In: *Journal of Tribology* 114.3 (July 1992), pp. 623–629. ISSN: 0742-4787. DOI: 10.1115/1.2920927. URL: https://asmedigitalcollection.asme.org/tribology/article/114/3/623/435641/A-Method-of-Separation-of-Variables-for-the.

[18]   T. Waumans et al. "Rotordynamic behaviour of a micro-turbine rotor on air bearings: Modelling techniques and experimental verification". In: *Proceedings of ISMA2006: International Conference on Noise and Vibration Engineering* 1 (2006), pp. 181–197.

[19]   J. W. (John William) Powell. *Design of aerostatic bearings.* Brighton, Machinery Pub., 1970, 280 pages. ISBN: 0853332045.

[20]   Abdurrahim Dal and Tuncay Karaçay. "Performance characteristics of an aerostatic journal bearing with partially blocked orifices:" in: *https://doi.org/10.1177/13506501211000592* 235.11 (Mar. 2021), pp. 2440–2454. ISSN: 2041305X. DOI: 10.1177/13506501211000592. URL: https://journals.sagepub.com/doi/full/10.1177/13506501211000592.

[21]   Gertjan van Zwieten, Joost van Zwieten, and Wijnand Hoitinga. "Nutils". In: (Jan. 2022). DOI: 10.5281/ZENODO.6006701. URL: https://doi.org/10.5281/zenodo.6006701#.YmKvm_Bb1Q1.mendeley.

[22]   N. S. Grassam. *Gas lubricated bearings.* London, Butterworths, 1964, xvi, 309 pages.

[23]   F. Wardle. *Ultra-precision Bearings.* Elsevier Science, 2015, 1 online resource. ISBN: 1322963118.

[24]   Xue Dong Chen, Jin Cheng Zhu, and Han Chen. "Dynamic characteristics of ultra-precision aerostatic bearings". In: *Advances in Manufacturing* 1.1 (Mar. 2013), pp. 82–86. ISSN: 21953597. DOI: 10.1007/S40436-013-0013-6/FIGURES/10. URL: https://link.springer.com/article/10.1007/s40436-013-0013-6.

[25]   Federico Colombo et al. "Evaluation of squeeze effect in a gas thrust bearing". In: *WIT Transactions on Engineering Sciences* 116 (Sept. 2017), pp. 121–130. ISSN: 1746-4471. DOI: 10.2495/MC170121. URL: http://www.witpress.com/elibrary/wit-transactions-on-engineering-sciences/116/36168.

[26]   Bruce C. Moore. "Principal Component Analysis in Linear Systems: Controllability, Observability, and Model Reduction". In: *IEEE Transactions on Automatic Control* 26.1 (1981), pp. 17–32. ISSN: 15582523. DOI: 10.1109/TAC.1981.1102568.

[27] Athanasios C (Athanasios Constantinos) Antoulas 1950-, Society for Industrial -, and Applied Mathematics. T A - T T. *Approximation of large-scale dynamical systems LK - https://tue.on.worldcat.org/oclc/693785925*. English. Philadelphia, Pa., 2005. URL: `http://epubs.siam.org/ebooks/siam/advances_in_design_and_control/dc06`.

[28] V. Simoncini. "A New Iterative Method for Solving Large-Scale Lyapunov Matrix Equations". In: *http://dx.doi.org/10.1137/06066120X* 29.3 (May 2007), pp. 1268–1288. ISSN: 10648275. DOI: `10.1137/06066120X`. URL: `https://epubs.siam.org/doi/abs/10.1137/06066120X`.

[29] Steven L Brunton and J Nathan Kutz. *Data-Driven Science and Engineering: Machine Learning, Dynamical Systems, and Control*. 2nd ed. Cambridge University Press, 2022. DOI: `10.1017/9781009089517`.

[30] René Milk, Stephan Rave, and Felix Schindler. "pyMOR – Generic Algorithms and Interfaces for Model Order Reduction". In: *http://dx.doi.org/10.1137/15M1026614* 38.5 (Oct. 2016), S194–S216. ISSN: 10957200. DOI: `10.1137/15M1026614`. arXiv: `1506.07094`. URL: `https://epubs.siam.org/doi/abs/10.1137/15M1026614`.

[31] Peter J. Schmid et al. "Applications of the dynamic mode decomposition". In: *Theoretical and Computational Fluid Dynamics* 25.1-4 (Aug. 2011), pp. 249–259. ISSN: 09354964. DOI: `10.1007/s00162-010-0203-9`.

[32] Peter J. Schmid. "Dynamic mode decomposition of numerical and experimental data". In: *Journal of Fluid Mechanics* 656 (Aug. 2010), pp. 5–28. ISSN: 14697645. DOI: `10.1017/S0022112010001217`.

[33] Shervin Bagheri et al. "Global stability of a jet in crossflow". In: *Journal of Fluid Mechanics* 624 (2009), pp. 33–44. DOI: `10.1017/S0022112009006053`.

[34] Joshua L. Proctor, Steven L. Brunton, and J. Nathan Kutz. "Dynamic mode decomposition with control". In: (Sept. 2014). arXiv: `1409.6358`. URL: `http://arxiv.org/abs/1409.6358`.

[35] Christophe Geuzaine and Jean-François Remacle. "Gmsh: a three-dimensional finite element mesh generator with built-in pre-and post-processing facilities". In: *International Journal of numerical methods in engineering Int. J. Numer. Meth. Engng* 0 (2009), pp. 1–24.

Appendices

Appendix A

Unstructured mesh results

To utilize the meshing and efficiency benefits of structured and uniform grids, that grid type has been used throughout the main content of this thesis. Nonetheless, the properties and perfomance of unstructured grids has been investigated, as the convergence of unstructered and uniform grids is bounded. The results obtained for unstructured meshes are reported in this appendix and compared to those of structured grids used in the main content.

The unstructred meshes are constructed using triangular elements using the default dimensions as listed in Table 3.1. The three-dimensional finite element mesh generator *Gmsh* is used for the meshing of unstructured meshes [35]. An example of such a mesh is illustrated in Figure A.1 for the half bearing geometry. A fundemental difference of this mesh type, in comparison with the structured meshes, is the fact that the orifices are now modeled as small but finite areas. For that reason the mesh density around the orifices is significantly higher.

A.1   Revision of the weak form

Because of the fact that a different modeling approach for the orifices is required, the entrance flow model, and additionally the weak form, should be revised accordingly. The source term of the Reynolds equation, which is given by Equation (2.9) in terms of the dirac delta function, is therefore rewritten in terms of the mass flow rate instead according to Equation (A.1)

$$\int_0^h q \mathrm{d}z = \frac{\dot{m}_j}{V_j} h_j = \frac{\dot{m}_j}{A_j} \tag{A.1}$$
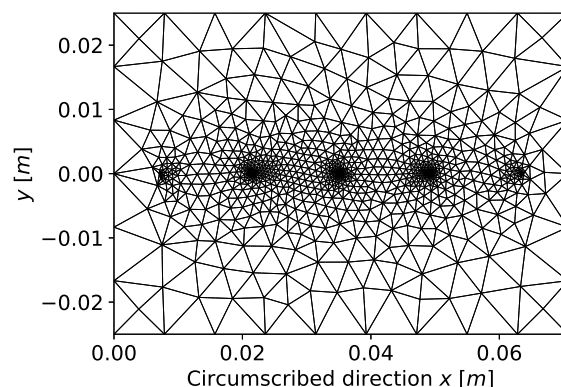

Figure A.1. *Example of an unstructured finite element mesh for the half bearing geometry.*

Where $\dot{m}_j$ is the mass flow rate through the jth orifice with area A_j. The expression for $\dot{m}_j$ as given in Section 2.2 still holds. The linear form of the weak form is altered accordingly, by applying this new source term as according to Equation (A.2). For this expression the same test and trial spaces are used as (2.20).

$$\mathcal{F}(\varphi) = \sum_{j=1}^{N} \int_{\Omega^{or}} \varphi \left(\Gamma Q_j \right) \mathrm{d}V \quad \forall \varphi \in \mathcal{V} \tag{A.2}$$

Where the the complete source term Q is written as:

$$Q = 12\mu R_s T_s \int_0^h q \, \mathrm{d}z = \sum_{j=1}^{N} 12\mu R_s T_s \frac{\dot{m}_j}{A_j} \tag{A.3}$$

A.2 Steady state results

Since the unstructured grids are not compatible with a b-spline basis, quadratic Bernstein basis functions are used for the discretization. Besides the above defined revisions, the same simulation is conducted as for the structured meshes. Figure A.2 reports the static pressure solution for eccentricity values $\varepsilon = 0.0$, 0.2, 0.4, 0.6. The results look very similar as those solved using a structured mesh depicted in Figure 3.3, in both the peak value of the pressure as well as its distribution.
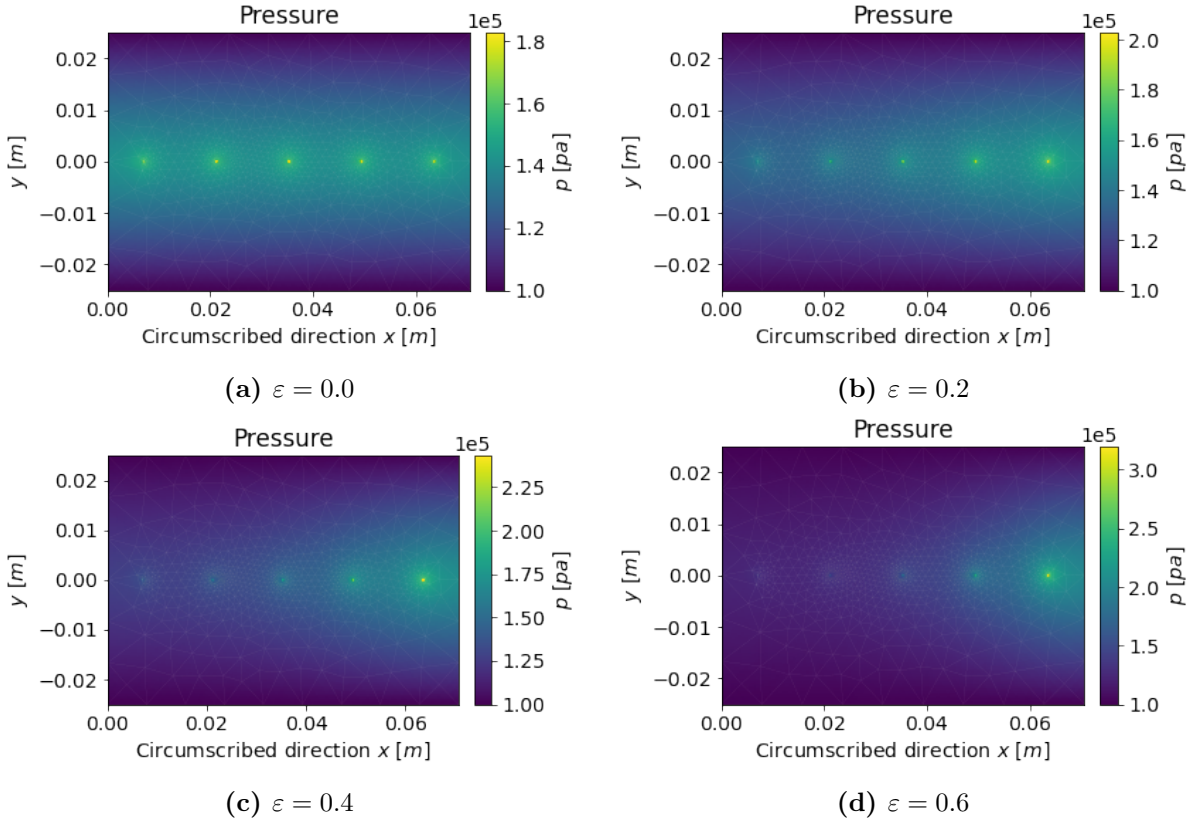

(a) $\varepsilon = 0.0$

(b) $\varepsilon = 0.2$

(c) $\varepsilon = 0.4$

(d) $\varepsilon = 0.6$

Figure A.2. *Steady state pressure distribution for increasing eccentricities and $\Lambda = 0.0$.*

1.2.1   Convergence of unstructred meshes

As proposed in Section 3.2, unstructured meshes may be utilised to conduct simulations with larger orifice diameters. Therefore, the convergence of these meshes is examined. Figure A.3 reports the convergence of the relative load capacity residual and the mass flow residual, using an orifice diameter of 0.18mm. This is about 10 orders of magnitude greater than the orifice geometry used throughout the main content. The relative load capacity residual in Figure A.3a shows decent performance in terms of rates and residual value. For the relative mass flow residual, however, the effect of the larger orifice diamer is visible. The rate is significantly lower and the residual values are realtively high.

To see the effects of such a bigger orifice to the pressure solution, a static solution is obtained using the orifice diameter of 0.18 mm. Figure Figure A.4 reports the static pressure solution for both $\varepsilon = 0.0$ and $\varepsilon = 0.4$. It can be seen that the pressure at the orifice approaches the supply pressure as the larger orifice diameter allows more mass to flow.
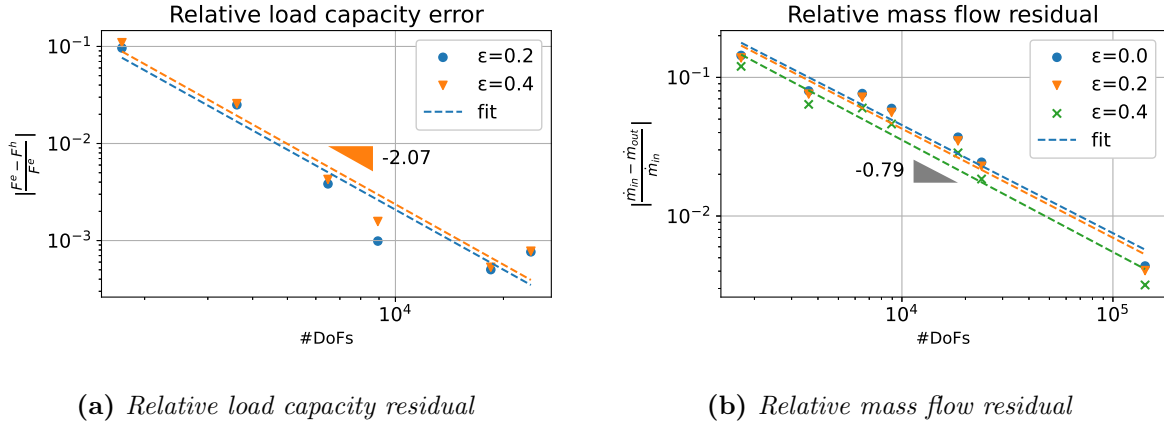

(a) *Relative load capacity residual*   (b) *Relative mass flow residual*

Figure A.3. *Convergence properties of the relative load capacity and the mass flow error using unstructured meshes.*

(a) *Vertical static load capacity*   (b) *Vertical static stiffness*
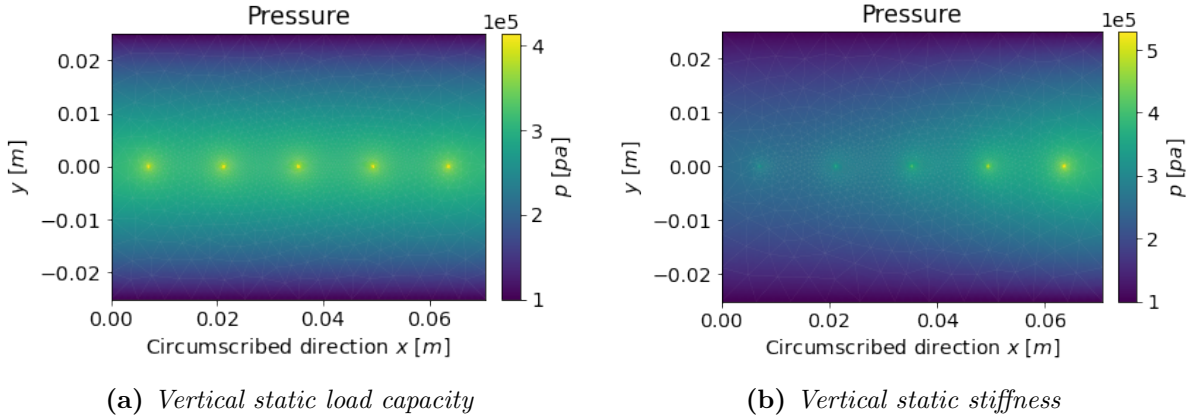
Figure A.4. *Steady state pressure solution solved with orifice diameter 0.18 mm for $\varepsilon = 0.0$ and $\varepsilon = 0.4$.*

Appendix B

State space representation of DMDc

DMDc is able to find two reduced order operators $\tilde{\mathbf{A}}$ and $\tilde{\mathbf{B}}$ that relates the snapshot matrices $\mathbf{X}'$ and $\mathbf{X}$ and the control input Υ best in time. By assigning a $\tilde{\mathbf{C}}$, the construction of a reduced order state space is allowed. Using the defined linearization from Chapter 4, $\tilde{\mathbf{C}}$ can be defined as:

$$\tilde{\mathbf{C}} = \hat{\mathbf{U}}\mathbf{C} \tag{B.1}$$

resulting in a state space realization of the DMDc, which according to Equation (4.9) can be written as a transfer function. To showcase this state space realization for the proposed air bearing model, the transient response at $\omega = 10^7$ is used to train the DMDc. The dynamic
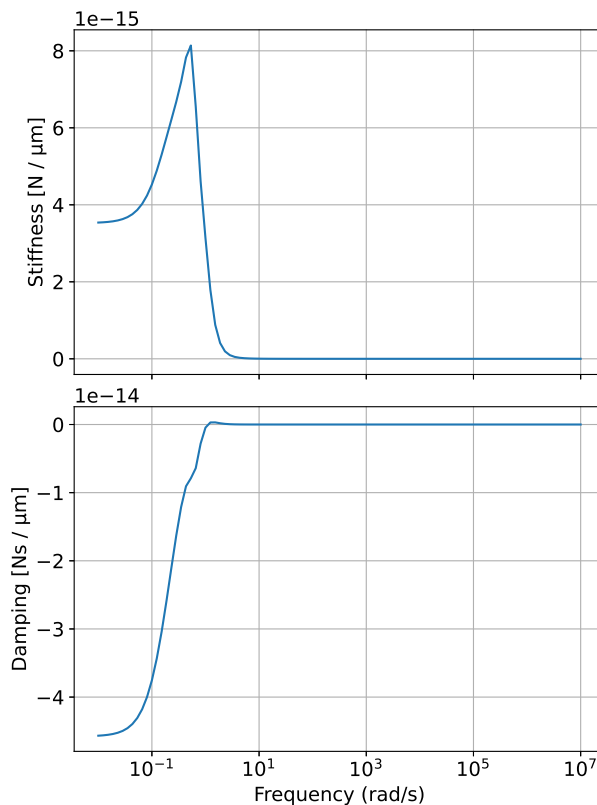

Figure B.1. *Poorly predicted dynamic characteristics obtained from the DMDc state space realization. The DMDc is trained at $\omega = 10^7$ and $\varepsilon = 0.0$.*

characteristics can be computed according to the method given in Section 4.1, the results of the DMDc state space representation are reported in Figure B.1. Because the DMDc is not able to capture the transient response per frequency, it is of no suprise that this poorly trained DMDc approximation is not able to predict the frequency dependent dynamic characteristics. However, given a proper trained DMDc, a convenient framework exists to couple the snapshot based DMDc with a system theoretic implementation.

Appendix C

Nonlinear Balanced Truncation

The goal of balanced truncation, transforming the system coordinates into its balanced form and subsequently obtaining a reduced-order-model, remains the same for nonlinear systems. However, in general this can only be achieved locally by a nonlinear coordinate transform.

Consider a smooth nonlinear system of the form:

$$
\begin{aligned}
\dot{x}(t) &= f(x(t)) + g(x(t))u(t), \\
y(t) &= h(x(t))
\end{aligned}
\tag{C.1}
$$

Additionally, zero is assumed to be an equilibrium, i.e. $f(0) = 0$ and $h(0) = 0$. The energy functionals defined by Scherpen are defined in analogy to the linear case as:

$$
\begin{aligned}
L_c\left(x_d\right) &= \min_{\substack{u \in L_2(-\infty, 0; \mathbb{R}^m) \\ x(-\infty)=0, x(0)=x_d}} \frac{1}{2} \int_{-\infty}^{0} u^T(t)u(t)\mathrm{d}t \\
L_o\left(x_0\right) &= \frac{1}{2} \int_{0}^{\infty} y^T(t)y(t)\mathrm{d}t, \quad x(0) = x_0, \quad u(t) \equiv 0, 0 \le t < \infty
\end{aligned}
\tag{C.2}
$$

While the Gramians P and Q of a linear system satisfy the linear matrix equations known as the Lyapunov equations, this does not hold for the nonlinear case. With suitable solvability assumptions the above defined L_c and L_o solve the following partial differential equations:

$$
\begin{aligned}
\frac{\partial L_C}{\partial x}(x)f(x) + \frac{1}{2}\frac{\partial L_c}{\partial x}(x)g(x)\left(\frac{\partial L_c}{\partial x}(x)g(x)\right)^T &= 0, \quad L_C(0) = 0 \\
\frac{\partial L_o}{\partial x}(x)f(x) + \frac{1}{2}(h(x))^T h(x) &= 0, \quad L_o(0) = 0
\end{aligned}
\tag{C.3}
$$

Using a nonlinear coordinate transform $x = \psi(\tilde{x}, \psi(0) = 0$, the following holds for the transformed balanced functionals.

$$
\begin{aligned}
\widetilde{L}_c(\tilde{x}) &:= L_c(\psi(\tilde{x})) = \frac{1}{2}\tilde{x}^T\tilde{x} \\
\widetilde{L}_o(\tilde{x}) &= L_o(\psi(\tilde{x})) = \frac{1}{2}\tilde{x}^T \operatorname{diag}\left(\sigma_1(\tilde{x}), \ldots, \sigma_n(\tilde{x})\right)\tilde{x}
\end{aligned}
\tag{C.4}
$$

It can be shown that a linearization of this approach yields the classical balancing technique applied to the linearization of the nonlinear system. Another approach for nonlinear balanced truncation is focused on replacing L_c and L_o by algebraic approximations, particularly for the class of bilinear systems.

C.1 Bilinear systems

Bilinear systems arise in several practical applications, but can also be used to approximate more general nonlinear systems by a Carleman linearization.

Consider a bilinear system as:

$$\dot{\chi}(t) = A\chi(t) + \sum_{i=1}^{m} N_i x(t) u_i(t) + Bu(t)$$

$$y(t) = C\chi(t)$$

(C.5)

The main advantage of using the algebraic gramians is that a global static coordinate transfrom can be used to transform the above bilinear system into balanced form and is completely analogous to the linear case.

Algorithm 2.3: Balanced truncation for bilinear control systems.

Require: Original system A, B, C and $N_1, \ldots, N_m$.

Ensure: Reduced system $\widehat{A}, \widehat{B}, \widehat{C}$ and $\widehat{N}_1, \ldots, \widehat{N}_m$.

1: Compute the solutions $X = L_X^T L_X$ and $Y = L_Y^T L_Y$ of (2.46).

2: Compute the SVD of $L_X L_Y^T$ as in (2.21).

3: Define $V = L_X^T U_1 \Sigma_1^{-\frac{1}{2}}$ and $W = L_Y^T Z_1 \Sigma_1^{-\frac{1}{2}}$.

4: Define $\widehat{A} = W^T A V$, $\widehat{B} = W^T B$, $\widehat{C} = CV$ and $\widehat{N}_i = W^T N_i V$, $i = 1, \ldots, m$.

Figure C.1. *Algorithm for bilinear balanced truncation from benner2021*